Article

Adipocyte-released adipomes in Chagas cardiomyopathy: Impact on cardiac metabolic and immune regulation

Trypanosoma cruzi | L- adipome | S- adipome

Adipocyte | Apoptotic adipocyte | M1 macrophage | M2 macrophage

Cardiomyocyte | Hypertrophied-cardiomyocyte | Fibroblast | Adipogenic Fibroblast

Hariprasad
Thangavel, Dhanya
Dhanyalayam,
Michelle Kim, ...,
Xiang Wang,
Shivani Bansal,
Jyothi F.
Nagajyothi

jyothi.nagajyothi@hmh-cdi.org

Highlights

T. cruzi triggers adipocyte apoptosis, releasing infection-specific adipomes

An innovative method for adipome isolation from circulation and adipose tissue

Infected mice's plasma adipomes carry unique lipids and regulate lipogenic genes

P-ILA-induced cardiomyopathy is associated with dysfunctional cardiac metabolism
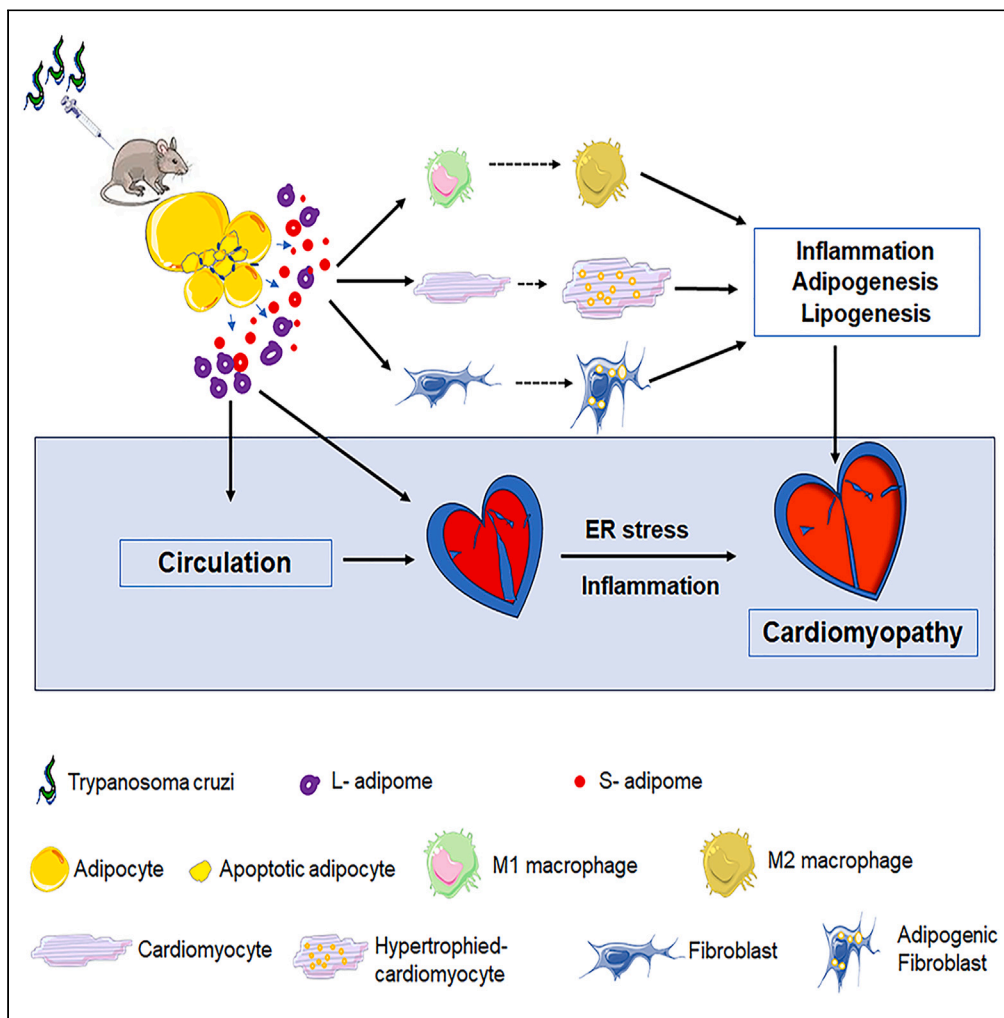
iScience

Article

Adipocyte-released adipomes in Chagas cardiomyopathy: Impact on cardiac metabolic and immune regulation

Hariprasad Thangavel,[1] Dhanya Dhanyalayam,[1] Michelle Kim,[1] Kezia Lizardo,[1] Tabinda Sidrat,[1] John Gomezcoello Lopez,[1] Xiang Wang,[2] Shivani Bansal,[3] and Jyothi F. Nagajyothi[1,4,*]

SUMMARY

Chronic _Trypanosoma cruzi_ infection leads to Chagas cardiomyopathy (CCM), with varying manifestations such as inflammatory hypertrophic cardiomyopathy, arrhythmias, and dilated cardiomyopathy. The factors responsible for the increasing risk of progression to CCM are not fully understood. Previous studies link adipocyte loss to CCM progression, but the mechanism triggering CCM pathogenesis remains unexplored. Our study uncovers that _T. cruzi_ infection triggers adipocyte apoptosis, leading to the release of extracellular vesicles named "adipomes". We developed an innovative method to isolate intact adipomes from infected mice's adipose tissue and plasma, showing they carry unique lipid cargoes. Large and Small adipomes, particularly plasma-derived infection-associated L-adipomes (P-ILA), regulate immunometabolic signaling and induce cardiomyopathy. P-ILA treatment induces hypertrophic cardiomyopathy in wild-type mice and worsens cardiomyopathy severity in post-acute-infected mice by regulating adipogenic/lipogenic and mitochondrial functions. These findings highlight adipomes' pivotal role in promoting inflammation and impairing myocardial function during cardiac remodeling in CD.

INTRODUCTION

Chagas disease (CD), caused by _Trypanosoma cruzi_, affects 8 million people in Latin America and 400,000 in the rest of the world, the latter mainly due to migration and blood transfusion.[1,2] Approximately 30% of infected individuals develop chronic symptomatic disease after several years or decades of initial infection, including dilated chronic cardiomyopathy (CCM), which can be fatal.[3] Furthermore, recent reports suggest that individuals in the acute phase can also progress to a chronic form of acute cardiomyopathy (ACM).[4] Acute infection may lead to generalized cardiac enlargement, affecting all four cardiac chambers, and may be accompanied by pericardial effusions.[5] While myocarditis arising during acute infection generally resolves with increased anti-inflammatory signaling in the heart, which is associated with cardiac remodeling, deregulated cardiac remodeling post-infection may contribute to the pathogenesis of Chagas cardiomyopathy, characterized by hypertrophied cardiomyopathy, dilated cardiomyopathy, and ultimately, heart failure. Although existing anti-parasitic drugs demonstrate significant efficacy in the early, acute CD stages, treatments available to prevent CCM are ineffective and have more severe side effects.[6]

The development of CCM is influenced by factors such as host metabolic and immunological status.[7] While pro-inflammatory signaling during acute infection contributes to myocarditis, CCM progression depends on cardiac energy metabolism, immune signaling, and the parasite's presence, regulating cardiac remodeling during the post-acute asymptomatic phase. Our studies of murine CD models have also revealed increased adipogenesis and altered lipid metabolism, as well as mitochondrial dysfunction, oxidative stress, and endoplasmic reticulum (ER) stress in the myocardium.[8–11] It has been shown that cardiac metabolic status influences the functions of heart immune cells and vice versa.[12] Thus, understanding the mechanism(s) promoting adipogenic/lipogenic signaling and mitochondrial dysfunction in the heart during cardiac remodeling is essential for the development of effective therapeutic interventions for CCM.

Adipose tissue (AT), which is mainly comprised of adipocytes, plays an important role in regulating whole-body immunity and metabolic homeostasis.[13–15] Cardiac AT is a dynamic organ with metabolic activity, actively participating in the maintenance of lipid and energy balance in the heart. Beyond serving as an energy source for the myocardium, it functions as a buffer protecting the heart from lipotoxicity, particularly in the presence of elevated circulating free fatty acids (FFAs).[16] We have shown that _T. cruzi_ invades adipocytes, whereupon AT serves as a parasite reservoir in both patients with CD and murine CD models.[17,18] _T. cruzi_ relies on adipocytes for cholesterol, as it cannot synthesize it independently.[19] Adipocytes provide nutrients for persistent _T. cruzi_ and facilitate the parasite evasion of host immunity.[20] Previously, we showed a strong correlation between loss of body fat and increased ventricular dilation in _T. cruzi_-infected mice.[17] Our studies also

[1]Center for Discovery and Innovation, Hackensack Meridian Health, Nutley, NJ 07110, USA
[2]Rutgers University Molecular Imaging Core (RUMIC), Rutgers Translational Sciences, Piscataway, NJ 08854, USA
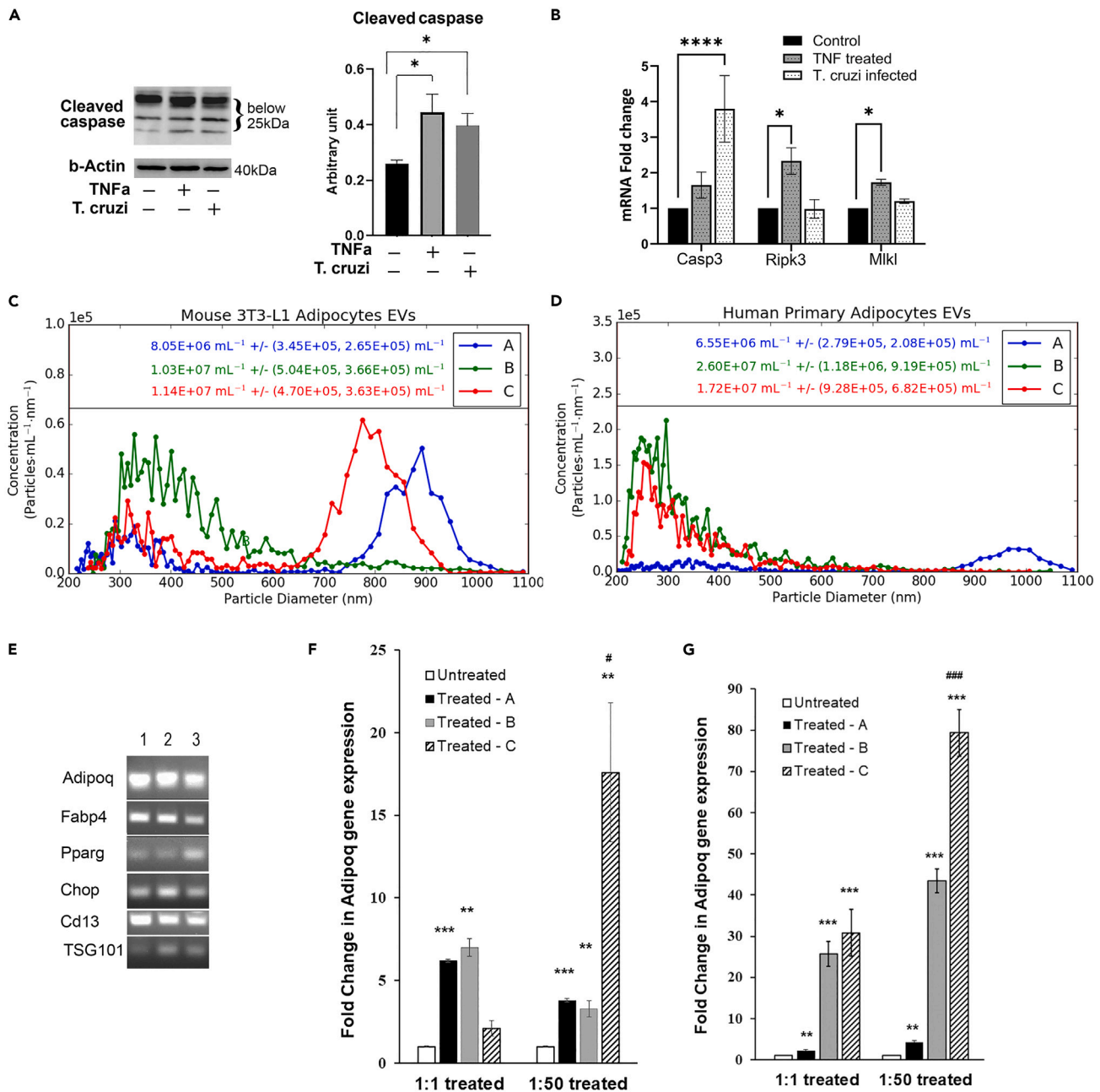[3]Department of Oncology, Lombardi Comprehensive Cancer Center, Georgetown University Medical Center, Washington, DC 20057, USA
[4]Lead contact
*Correspondence: jyothi.nagajyothi@hmh-cdi.org
https://doi.org/10.1016/j.isci.2024.109672

Figure 1. *T. cruzi* **infection induces adipocyte apoptosis, releasing adipomes that regulate adipogenic signaling**

(A) Immunoblot analysis of cleaved Caspase 7 expression in the lysates of 3T3-L1 adipocytes (uninfected, TNFα-treated, and *T. cruzi* infected) ($n = 3$/group). Bar graph values were derived from densitometry analysis and by normalizing target protein expression to β-Actin.

(B) Fold change expression of *CASP3*, *RIPK3*, and *MLKL* mRNA transcripts (normalized to *HPRT*) in cultured human adipocytes (uninfected, TNFα-treated and *T. cruzi* infected) ($n = 3$).

(C and D) Adipome size distribution and absolute concentration as determined by Spectradyne nCS1 with a C-900 microfluidic cartridge. Both mouse and human adipomes were derived from cultured 3T3-L1 and human adipocyte-conditioned media, respectively. Inset: A (blue) = uninfected, B (green) = TNFα-treated, C (red) = *T. cruzi* infected.

(E) PCR analysis of adipogenic (*Adipoq*, *Fabp4*, and *Pparg*), apoptotic (*Chop*) and extracellular vesicle (*Tsg101* and *Cd13*) marker genes in 3T3-L1-derived adipomes. Lane 1, 2, and 3 represent 3T3-L1-derived adipomes from three independent cultures. Product size: *Adipoq*, 192bp; *Fabp4*, 133bp; *Pparg*, 132bp; *Chop*, 118bp; *Tsg101*, 103bp; and *Cd13*, 121bp.

(F and G) Fold change expression of *Adipoq* mRNA transcripts (normalized to *Hprt*) in RAW macrophages (F) and human fibroblasts (G) treated with 3T3-L1- and human adipocyte-derived adipomes, respectively, at 1:1 and 1:50 cell-to-adipome ratio for 48 h ($n = 3$). All treatment groups (Treated - A, - B and - C) were

Figure 1. Continued

compared to untreated groups. The # symbol indicates comparison between Treated - B and - C. Treated - A = adipomes from uninfected adipocytes; Treated - B = adipomes from TNFα-treated adipocytes; and Treated - C = adipomes from *T. cruzi*-infected adipocytes. Data are represented as mean ± SEM. (*/#$p < 0.05$, **$p \leq 0.01$, ***/###$p \leq 0.001$ and ****$p \leq 0.0001$).

demonstrated that *T. cruzi* persistence in AT disrupts host lipid metabolism, increasing CCM risk by causing adipocyte cell death.[11] Our prior studies of murine CD models have revealed a connection between the loss of body fat resulting from induced adipocyte apoptosis and an escalation of cardiomyopathy.[11] This association was observed during both the acute and indeterminate stages of *T. cruzi* infection, indicating a crucial role for pathological adipocytes in the regulation of cardiomyopathy in CD.[11] In this study, our primary objective was to elucidate the immunometabolic consequences of adipocyte apoptosis and its impact on cardiac remodeling, which in turn influences the pathogenesis of cardiomyopathy in CD.

Building upon our previous findings, we developed a hypothesis that *T. cruzi* infection induces the apoptosis of adipocytes, leading to the release of extracellular vesicles, a.k.a. "adipomes", and that these adipomes may regulate the immune and metabolic functions of the myocardium, heightening the risk of cardiomyopathy during *T. cruzi* infection. The current study utilized both *in vitro* and *in vivo* models to test this hypothesis by investigating how pathological adipocyte-derived adipomes regulate immune cell activation and cardiomyocyte dysfunction in post-acute *T. cruzi* infection state. To isolate intact adipomes from the plasma and AT of infected mice, we developed an innovative method where the adipomes could be selectively purified based on their size (large (L) or small (S)) and unique surface markers. This purification method overcomes the limitations in isolating adipocyte-specific adipomes from AT in its microenvironment.[21,22] We characterized the adipomes using transmission electron microscopy (TEM) and analyzed their lipid contents, showing that they contained active lipid biomolecules whose patterns varied between adipomes derived from healthy versus pathological adipocytes. Additionally, we assessed the functional significance of L-adipomes isolated from the plasma of *T. cruzi*-infected mice by injecting them into the hearts of wild-type and post-acute Chagas mice. We observed that adipome treatment increased inflammatory and adipogenic/lipogenic signaling and markers of ER stress, as well as elevated levels of atrial natriuretic peptide (ANP) and β1-adrenergic receptor (β1-AR) in the mouse hearts. Finally, we found that the ultrasound-guided intramyocardial injection of plasma-derived infection-associated L-adipomes (P-ILA) significantly altered cardiac morphology, increasing the risk of cardiomyopathy in wild-type mice compared to treatment with the vehicle alone. Together, these findings offer new mechanistic insights into the immune and metabolic alterations triggered by the *T. cruzi* infection of AT that regulate cardiac remodeling and promote cardiac pathogenesis during CD.

RESULTS

In our previous studies, we reported several key findings, including: (i) a significant correlation between the loss of body fat (adipocytes) and ventricular dilation,[17] (ii) an elevated risk of cardiomyopathy during both acute and chronic stages and a correlation with adipocyte apoptosis,[11] and (iii) the involvement of adipogenic/lipogenic signaling associated with ER stress in the pathogenesis of chronic dilated cardiomyopathy in *T. cruzi*-infected mice.[9,10] Together, these data suggested a link between adipocyte apoptosis and the pathogenesis of cardiomyopathy. However, the mechanism by which dying adipocytes may contribute to the risk of cardiomyopathy was not well understood. In this study, we investigated whether extracellular vesicles released by adipocytes under pathological conditions, elevate the risk of cardiomyopathy by regulating heart muscle cells. We also proposed that these adipomes may exert paracrine and endocrine effects on various cell types in the myocardium, including resident and infiltrated immune cells. To systematically test our hypothesis, we isolated adipomes from cultured adipocytes and developed an innovative method to isolate circulating and AT-derived adipomes from mice acutely infected with *T. cruzi*. Subsequently, we conducted comprehensive *in vitro*, *ex vivo*, and *in vivo* functional analyses. The detailed results are provided later in discussion.

T. cruzi infection of cultured adipocytes leads to apoptosis and the release of adipomes

To test our hypothesis, we investigated whether the *T. cruzi* infection of adipocytes during the early stage of infection (when most trypomastigotes invade adipocytes in culture, transform into amastigotes, and initiate replication) triggers adipocyte apoptosis and induces the release of extracellular vesicles (adipomes). We used cultured murine and human adipocytes infected with *T. cruzi* (MOI 3:1) for 72 h and analyzed protein and mRNA levels of apoptosis markers in murine and human adipocytes, respectively. The levels of apoptosis marker, cleaved caspase7 was measured in cell lysates from *T. cruzi*-infected and uninfected murine 3T3-L1 differentiated adipocytes. As a positive control for apoptosis, we treated 3T3-L1 adipocytes with TNFα for 48 h.[23] Immunoblotting analysis revealed significantly higher levels of cleaved caspase in *T. cruzi*-infected and TNFα-treated adipocytes compared to uninfected cells, indicating that *T. cruzi* infection induces apoptosis in adipocytes (Figure 1A). Similarly, qPCR analysis demonstrated a significant increase in *CASP3* gene expression in *T. cruzi*-infected human adipocytes compared to uninfected cells (Figure 1B). The levels of necroptotic gene markers such as *RIPK3* and *MLKL* were not altered in *T. cruzi*-infected cells, but were significantly increased in TNFα-treated cells compared to untreated human adipocytes (Figure 1B).

Next, we investigated whether *T. cruzi* infection-induced apoptosis resulted in the release of adipocyte-specific extracellular vesicles (adipomes). We isolated adipomes from the conditioned medium using the Exoquick-TC Ultra EV isolation kit (Figure S1A) and quantified their size distribution and concentration using Spectradyne nCS1 instrument. The size of adipomes ranged between 200 nm and 1100 nm for both cultured 3T3-L1 murine adipocytes and human adipocytes (Figures 1C and 1D). The adipomes derived from uninfected and *T. cruzi*-infected 3T3-L1 adipocytes showed two distinct peaks corresponding to sizes ranging from 200 nm to 400 nm and 600 nm–1000 nm, whereas the
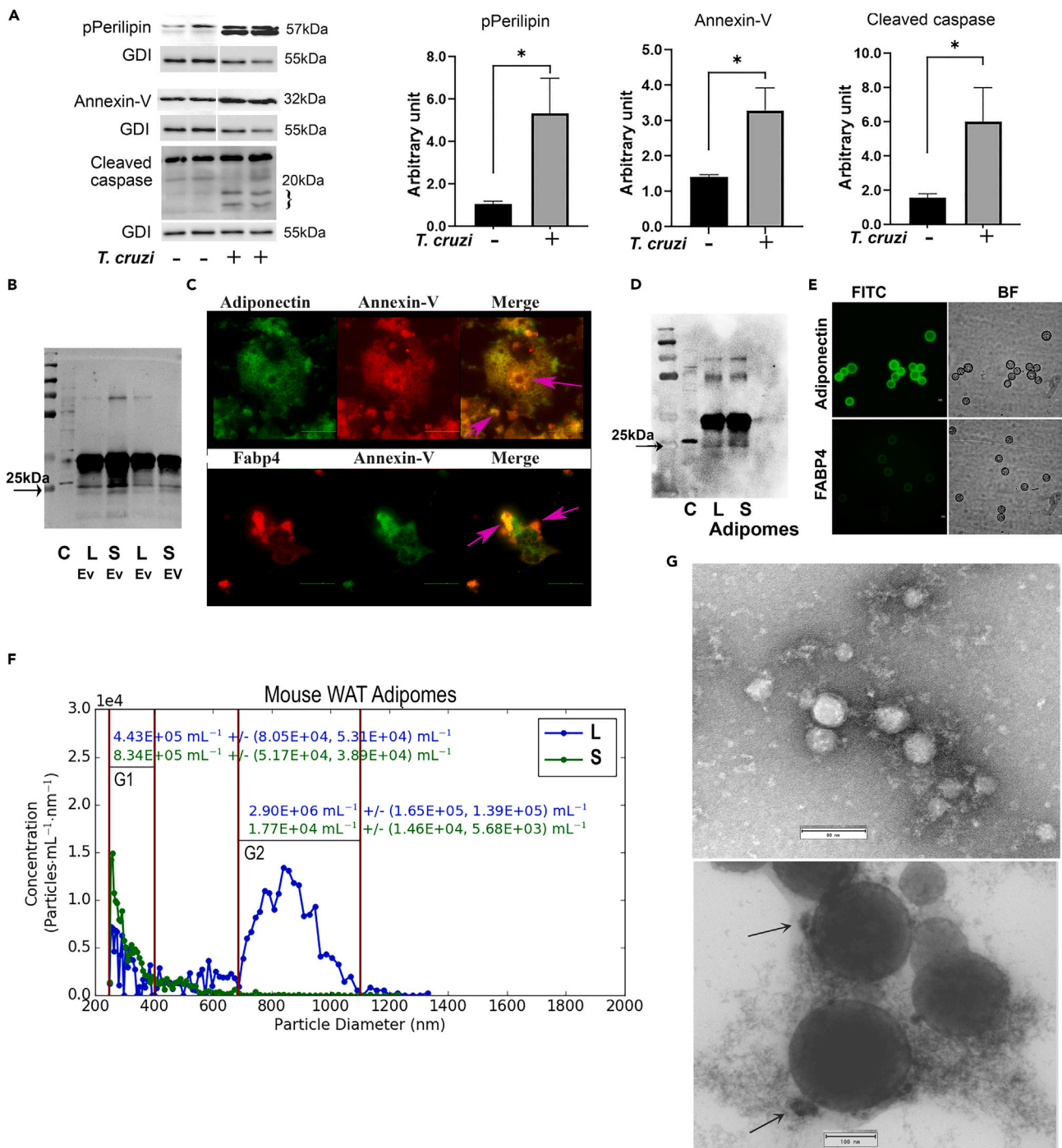
Figure 2. Adiponectin enables selective capture of adipomes from murine white adipose tissue (WAT)

(A) Immunoblot analysis of phospho-Perilipin, cleaved Caspase 7 and Annexin V expression in the WAT lysates of infected (20 DPI) and uninfected C57BL/6J mice (n = 4–8 per group). Bar graph values were derived from densitometry analysis and by normalizing target protein expression to GDI. Error bars indicate the standard error of the mean (*$p < 0.05$).

(B) Immunoblot analysis of adiponectin in WAT-derived large-EVs (L-EV) and small-EVs (S-EV). Black arrow points to the 25 kDa marker band on the pre-stained protein ladder. Adiponectin band appears at 26/30 kDa. Lanes: C, control WAT lysate; L Ev, large-EV; and S Ev, small-EV.

(C) Surface immunofluorescence staining of 3T3-L1 adipocytes show the co-localization of Adiponectin (green) with Annexin V (red) (top panel) and FABP4 (red) with Annexin V (green) (bottom panel) on budding apoptotic bodies. Scale bar, 50 μm.

Figure 2. Continued

(D) Immunoblot analysis of adiponectin in WAT-derived large-adipomes and small-adipomes. Black arrow points to the 25 kDa marker band on pre-stained protein ladder. Adiponectin band appears at 26/30 kDa. Lanes: C, control WAT lysate; L, large-adipomes; and S, small-adipomes.

(E) Immunofluorescence assay (IFA) of bead-bound adipomes stained with Adiponectin-AF488 (top panel) and FABP4-AF488 (bottom panel) imaged on the FITC channel along with their corresponding bright field (BF) images. Scale bar, 5 μm.

(F) WAT-derived adipome size distribution and absolute concentration as determined by Spectradyne nCS1 with a C-2000 microfluidic cartridge. Inset: L (blue), large-adipomes; S (green), small-adipomes. Gate: G1, particle concentration at size range of 250–400 nm diameter showing more small-adipomes than large-adipomes; and G2, particle concentration at size range of 700–1100 nm diameter showing mostly large-adipome distribution.

(G) Transmission Electron Microscopy (TEM) images of small-adipomes (left, scale bar 80 nm) and large-adipomes (right, scale bar 100 nm) with a direct magnification of 20,000×. Black arrow indicates the budding scars on L-adipomes.

adipomes from TNFα-treated 3T3-L1 adipocytes were mostly between 300 nm and 500 nm (Figure 1C). Adipomes derived from *T. cruzi*-infected and TNFα-treated human adipocytes mostly ranged between 200 nm and 400 nm (Figure 1D). The number of adipomes released from *T. cruzi*-infected and TNFα-treated adipocytes (in both murine and human adipocytes) were significantly higher (1.4-fold–2.8-fold) compared to the adipomes released from uninfected adipocytes. These findings indicated that *T. cruzi* infection leads to adipocyte apoptosis and that apoptotic adipocytes produce higher levels of adipomes than healthy adipocytes.

### Cultured adipocyte-derived adipomes regulate adipogenic signaling in macrophages and fibroblasts

We performed qPCR analysis of adipomes and found that adipomes contain adipogenic (*Adipoq, Fabp4, Pparg*), apoptotic (*Chop*), and extracellular vesicle (*Cd13* and *Tsg101*) gene mRNAs (Figure 1E). Thus, adipomes may influence adipogenic signaling in target cells, such as macrophages and fibroblasts. To test this hypothesis, first, we treated RAW 264.7 macrophages with adipomes obtained from murine 3T3-L1 cells at two different cell-to-adipome ratios (1:1 and 1:50). Second, we treated human foreskin fibroblast (HFF) cells with adipomes derived from cultured human adipocytes. Adipomes were isolated from uninfected adipocytes, *T. cruzi*-infected adipocytes, and adipocytes treated with TNFα (as a positive control for apoptosis).[23] Subsequently, we analyzed the gene expression in the target cells by qPCR analysis. Our findings have revealed that, in macrophages treated with adipomes derived from *T. cruzi*-infected adipocytes, the mRNA levels of adiponectin were significantly upregulated in the 1:50 treatment compared to naive macrophages (Figure 1F). In HFF cells, adiponectin levels were significantly upregulated in both 1:1 and 1:50 adipome-treated cells compared to naive HFF cells. Additionally, this upregulation was observed in cells treated with adipomes from control or TNFα-treated adipocytes (Figures 1F and 1G). Furthermore, to investigate the effects of upregulated adiponectin expression, we quantified the mRNA levels of adiponectin receptors (*Adipor1* and *Adipor2*), *Ppara*, and *Tnfa*, all of which are regulated by adiponectin. Our observations showed that *Ppara* and *Adipor2* levels were significantly upregulated in macrophages incubated with adipomes (1:50) from *T. cruzi*-infected and TNFα-treated adipocytes compared to naive macrophages and those treated with adipomes from control adipocytes (Figure S1B). However, in HFF cells incubated with adipomes (1:50) from *T. cruzi*-infected adipocytes, the levels of *Ppara* and *Adipor2* were significantly downregulated compared to untreated HFF cells and those treated with adipomes from control and TNFα-treated adipocytes (Figure S1C).

Together, these experiments demonstrate that adipomes in general and adipomes from *T. cruzi*-infected adipocytes in particular upregulate adiponectin gene expression in macrophages and fibroblasts in a concentration-dependent manner. Additionally, the adipomes either have no effect or downregulate Tnfa in macrophages. Finally, adipomes differentially regulate the gene expression of *Ppar*s, *Adipor1*, and *Adipor2* in macrophages and HFF cells.

Acute *T. cruzi* infection promotes the release of L-adipomes in mouse AT

Our *in vitro* data on the regulatory role of culture adipocyte-derived adipomes in macrophages and fibroblasts (Figures 1F and 1G) suggested that adipomes derived from AT may play a critical role in regulating major myocardial cells during *T. cruzi* infection *in vivo*. To begin to address this question, we investigated whether adipocytes of infected mice release adipomes. In a previous study, we demonstrated that during acute infection with *T. cruzi*, there was an increase in the infiltration of immune cells and pro-inflammatory signaling in both white and brown AT.[24,25] We also showed a significant loss of adipocytes during acute infection.[17,26] When considering the production of pathological adipocytes and adipocyte-derived adipomes during *T. cruzi* infection, it is important to note that mice lack a true epicardial fat depot. Instead, they possess a small fat deposit around the heart,[27,28] which is too small to isolate adipomes. Moreover, pericardial fat is rarely found in the acute Chagas mouse model, as we observed in the MRI images from our previous study, which showed the disappearance of pericardial fat during acute infection (Figure S2A). Consequently, in this study, we chose to focus on visceral fat pads (epididymal white adipose tissue (WAT). First, we investigated whether *T. cruzi* infection induces apoptosis in WAT, leading to the loss of adipocytes and subsequent release of adipomes. Indeed, immunoblotting analysis of WAT revealed elevated levels of markers of lipolysis (phospho-Perilipin) and apoptosis (cleaved caspase 7 and Annexin V) in *T. cruzi*-infected mice compared to uninfected mice (Figure 2A). These findings suggest that, as in cell culture, the *T. cruzi* infection of AT triggers adipocyte apoptosis and may lead to the release of apoptotic bodies and other macrovesicles.

It is well-known that large/macro EVs (large-EVs), such as ApoBDs and macrovesicles, differ in size and mechanism of origin from small or micro extracellular vesicles (small-EVs), such as microvesicles and exosomes.[29–33] Therefore, in order to investigate the specific role of pathological adipocyte-derived adipomes in CD pathogenesis, we isolated and separated large- and small-EVs from WAT based on their size using high-speed centrifugation, as detailed in the STAR Methods. We observed that the levels of large-EVs were significantly higher in the WAT of infected mice (ranging between 2 and 10x10^7/100mg) compared to uninfected mice (ranging between 5 and 10x10^5/100mg),
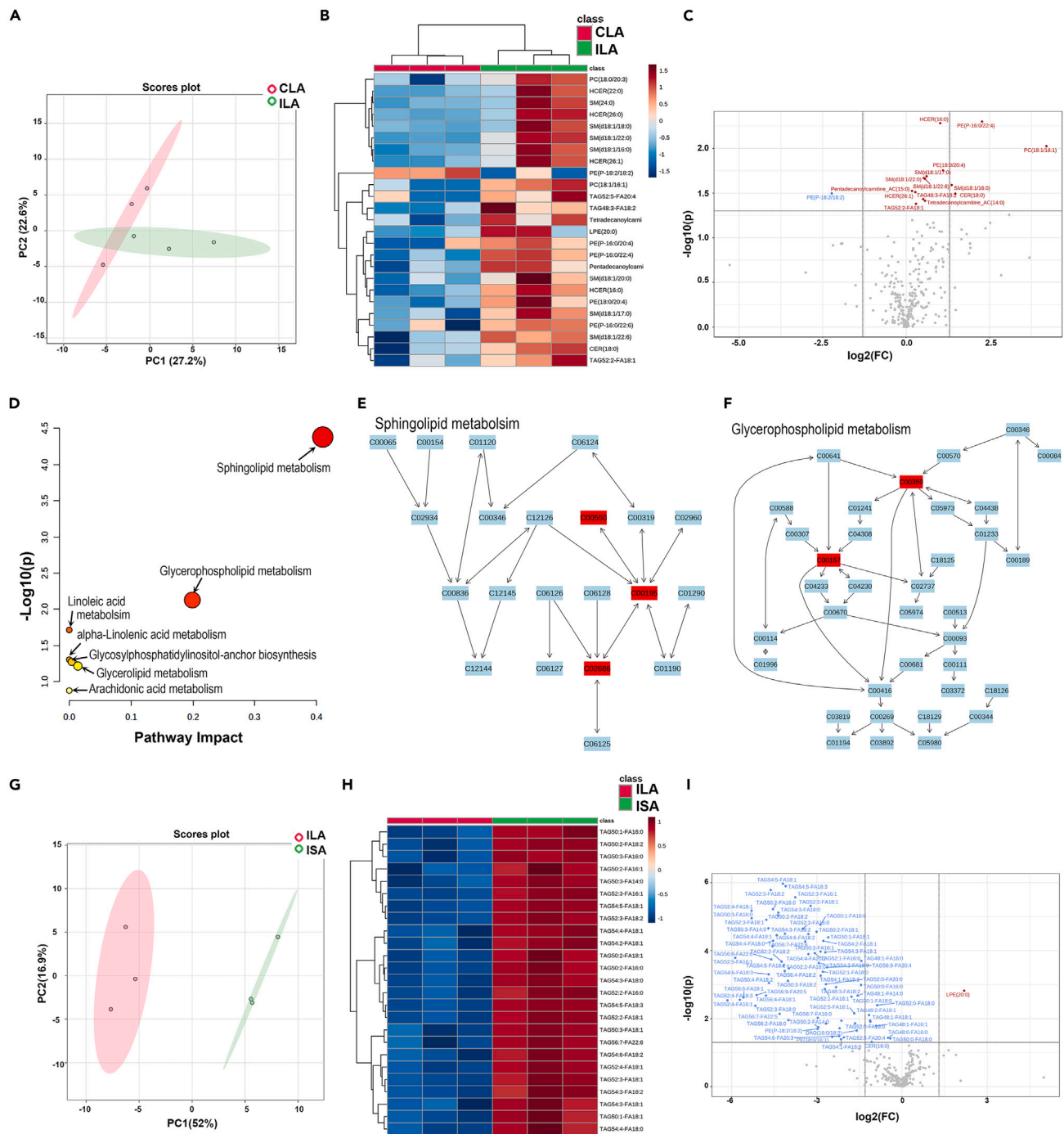
Figure 3. The lipidome of L-adipomes is distinct from that of S-adipomes

(A and G) Principal component analysis (PCA) score plot of the lipid profiles from CLA and ILA (A), and ILA and ISA (G) showing clusters of two groups.

(B and H) Heatmap representation of the clustering analysis of top 25 differentially abundant lipid molecular species (with lowest FDR-adjusted *p*-values) based on z-scores for the normalized, transformed, and scaled data between CLA and ILA (B), and ILA and ISA (H). For class names, red represents CLA or ILA and green represents ILA or ISA. For the abundance of each lipid, red represents high, and blue represents low.

(C and I) Volcano plots represent significantly altered lipid metabolites in ILA compared to CLA (C), and ISA compared to ILA (I). Red dots indicate upregulated lipids and blue dots indicate downregulated lipids.

(D) KEGG pathway analysis revealed seven dysregulated metabolic pathways enriched in ILA compared to CLA. All matched pathways were plotted according to *p*-value and pathway impact score from pathway enrichment analysis and pathway topology analysis, respectively. Color gradient: yellow, higher *p*-value; and red, lower *p*-value. Circle size: large, higher impact score; and small, lower impact score.

Figure 3. *Continued*

(E and F) Pathway representation of Sphingolipid metabolism (E) and Glycerophospholipid metabolism (F) with lipid metabolites (highlighted in red) enriched in ILA. Data represents the mean (*n* = 3 per group). Abbreviations: CLA, control large-adipomes; ILA, infected large-adipomes; and ISA, infected small-adipomes.

as quantitated by the Exocet exosome quantification kit (System Biosciences) with *p*-value ≤0.05. However, the levels of small-EVs did not show any significant difference between uninfected and infected mice, with counts ranging from 2.0 to 3.0x10^{8}. Additionally, immunoblotting analysis revealed the presence of the adipocyte-specific marker, adiponectin, in both large-EVs and small-EVs (Figure 2B).

Developing an innovative method to isolate intact adipomes from mouse WAT

In the body, AT is comprised not only of adipocytes, but also various other cell types, including immune cells, that may contribute to the overall extracellular vesicle (EV) pool. Thus, to develop a method to specifically isolate adipomes derived from adipocytes, we investigated the suitability of adiponectin and FABP4, two widely used adipocyte markers, as surface markers that can be utilized for affinity purification. First, we investigated whether apoptosis regulates the expression of adiponectin and FABP4, and whether adiponectin and/or FABP4 are present on the cell surface of apoptotic adipocytes. We used murine 3T3L1 differentiated adipocytes (treated with TNFα for 24 h) and performed surface immunofluorescence analysis (IFA). Our observations revealed the co-localization of adiponectin and FABP4 with Annexin V (apoptosis marker) on the surface of budding apoptotic bodies (Figures 2C and S2B). Annexins are present on the surface of EVs.[34–37] Based on this *in vitro* data and previous studies demonstrating the presence of adiponectin and FABP4 in adipocyte-derived EVs,[38] we selected adiponectin and FABP4 as markers to isolate adipocyte-specific EVs/adipomes from the total pool of WAT-derived EVs.

Next, we successfully enriched intact L-adipomes (large-adipomes) and S-adipomes (small-adipomes) from large-EVs and small-EVs, respectively, following the procedure described (Figure S1A). Immunoblotting analysis confirmed the presence of adiponectin, FABP4, Annexin V, and perilipin in both L- and S-adipomes, providing further evidence of their adipocyte origin (Figures 2D and S2C). Moreover, surface immunostaining of bead-bound adipomes provided additional support for the use of adiponectin and FABP4 as suitable markers for identifying and isolating adipomes from a pool of EVs (Figure 2E). Fluorescence microscopic analysis revealed a stronger green fluorescence intensity in adipomes stained for surface adiponectin compared to FABP4-stained adipomes, indicating that adiponectin is more abundant on the surface of adipomes compared to FABP4 (Figure 2E). As a negative control, we also stained the magnetic streptavidin beads to check for autofluorescence or non-specific antibody binding and found no fluorescence signal (Figure S2D). Further characterizations of adipomes included determining their size distribution and abundance using Spectradyne nCS1 (Figure 2F) and examining their size and integrity through TEM analysis (Figures 2G and S2E–S2G). Spectradyne measurements produced distinct peaks for L- and S-adipomes (Figure 2F), while TEM images of L-adipomes exhibited the presence of apoptotic budding scars, with a size range between 200 and 400 nm. In contrast, the size of S-adipomes ranged between 30 and 80 nm, as shown by TEM images (Figures 2G and S2E–S2G). These findings validate our innovative method for isolating adipocyte-specific adipomes from WAT.

L-adipomes and S-adipomes carry a distinct set of lipid cargoes, which differ between uninfected and infected mice

Adipocytes in WAT contain large amounts of lipids compared to other cells.[39] During infection, the presence of parasites may alter adipocyte lipid composition. Thus, adipomes may also carry a substantial amount of lipid biomolecules, and their lipid contents may vary between infected and uninfected mice. To investigate whether the lipid cargoes differ between large adipomes (L-adipomes) and small adipocytes (S-adipomes) and between pathological and normal conditions (infection vs. non-infection), we conducted Liquid Chromatography-Mass Spectrometry-based lipidomics analysis of L-adipomes and S-adipomes derived from WAT of control (uninfected) mice (CLA and CSA, respectively) and infected mice (ILA and ISA, respectively). A total of 287 lipid metabolites were identified, covering more than 21 subclasses including free cholesterol, free fatty acids (FFA), sphingomyelins (SM), phospholipids, ceramides (CER), triglycerides (TAG), and so forth. These lipids were quantified using class-specific internal standards (see STAR Methods). The lipidomic analysis of CLA, ILA, CSA, and ISA revealed diverse lipid patterns specific to the pathological conditions and the two types of adipomes (large vs. small) (Figures 3 and S3). For example, cholesterol levels were higher in ILA and ISA compared to CLA and CSA, while total FFA levels were lower in ILA and ISA compared to CLA and CSA. Additionally, total diacylglycerol (DAG) and TAG levels were greater in ISA compared to all other groups (Figure S3A). ILA contained higher levels of total ceramides, hydroxy ceramides (HCER), SM, and various phospholipids compared to CLA (Figure S3A).

Even in cases where specific lipid classes were not significantly altered between the groups, the levels of many individual lipid metabolites within each class were differentially expressed (DE) and specific to CLA, CSA, ILA, and ISA (the complete list of DE lipid metabolites in CLA, CSA, ILA, and ISA are available in Table S1). Further analysis comparing CLA and ILA showed significant differences in several lipid metabolites between these two groups (Figures 3A–3C). We applied Principal component analysis (PCA) to identify the metabolic profile differences between groups (Figure 3A). First, a heatmap was used to find the relative intensity distribution of the significantly altered lipid metabolites and to identify differentially expressed lipid metabolites between CLA and ILA, as shown in Figure 3B. We next constructed a volcano plot applying a significance *p*-value level of <0.05 based on t-test and a fold change (FC) value higher than 1.5 (Figure 3C). The volcano plot analysis revealed 15 lipid molecular species significantly altered in ILA relative to the CLA group. Notably, levels of PC(18:1/16:1), PE(18:0/20:4), PE(P-16:0/22:6), HCER(16:0), HCER(26:1), SM(d18:1/22:0), SM(d18:1/22:6), SM(d18:1/17:0), SM(d18:1/16:0), CER(18:0), pentadecanoyl

Table 1. Upregulated Metabolites in ILA compared to CLA and their respective KEGG metabolite ID

| Metabolites	KEGG
PC(14:0/20:2)	C00157
Ceramide (d18:1/18:0)	C00195
TG(16:0/18:0/18:2)	C00422
PE(O-16:1/22:6)	C00350
PE(16:0/22:4)	C00350
Galactosylceramide (d18:1/16:0)	C02686
Galactosylceramide (d18:1/26:1)	C02686
SM(d18:1/22:0)	C00550
SM(d18:0/16:1(OH))	C00550
SM(d18:0/16:1)	C00550

Related to Figure 3.

carnitine-AC (15:0), tetradecanoyl AC (14:0), TAG48:3-FA18:2, and TAG52:2-FA18:1 were significantly increased, while levels of PE(P-18:2/18:2) were significantly decreased in ILA compared to CLA (Figure 3C).

To identify the molecular mechanisms associated with the lipid metabolites enriched in ILA compared to CLA, we employed the Pathway Topology Analysis (PTA) module. The PTA module combines powerful pathway enrichment analysis with pathway topology analysis to identify the most relevant pathways altered by the metabolites (see STAR Methods). Pathway Analysis of the upregulated lipid metabolites in ILA compared to CLA revealed that the enriched lipid metabolites in ILA are involved in seven different lipid signaling pathways, including Sphingolipid metabolism, Glycerophospholipid metabolism, Linoleic acid metabolism, alpha-Linolenic acid metabolism, Glycosylphosphatidylinositol (GPI)-anchor biosynthesis, Glycerolipid metabolism, and Arachidonic acid metabolism (Table 1; Figure 3D). Based on the KEGG numbers of lipid metabolites, we identified five metabolites involved in Sphingolipid metabolism (such as SM(d18:1/22:0) [KEGG# C00550], SM(d18:0/16:1 [KEGG# C00550], SM(d18:0/16:1 [KEGG# C00550]), Galactosylceramide (d18:1/16:0) [KEGG# C02686], and Galactosylceramide (d18:1/26:1) [KEGG# C02686]), three metabolites in Glycerophospholipid signaling (such as PC(14:0/20:2 [KEGG# C00157]), PE(O-16:1/22:6) [KEGG# C00350], and PE(16:0/22:4) [KEGG# C00350]), and one metabolite in Linoleic acid pathway PC(14:0/20:2 [KEGG# C00157]) (Figures 3E and 3F; Table S2). Impaired accumulation of these metabolites and associated pathways has been shown to increase the risk of cardiovascular and coronary artery diseases.[40,41] Thus, these analyses suggest that the interaction of cardiomyocytes with ILA may impair cardiomyocyte functions through alterations in sphingolipid, glycerophospholipid, and linoleic acid metabolisms.

We also compared lipid metabolite levels between ILA and ISA to identify any differences in lipid contents between the large and small adipomes derived from infected mice (Figures 3G–3I). The PCA revealed a clear separation between the two groups (ILA and ISA) (Figure 3G), and we observed differentially expressed metabolites between ILA and ISA samples (Figure 3H). Specifically, the levels of various TAGs (more than 50) were significantly decreased in ILA compared to ISA, with the exception of LPE (20:0), which was significantly higher in ILA (Figure 3I). Similarly, we observed differences in DE lipid metabolites between ISA and CSA (Figures S3B and S3C). Notably, the levels of various TAGs were significantly higher in ISA compared to CSA (Figure S3C). This data further supports the idea that ISAs are rich in TAGs, which may be important in how they regulate cellular functions. Furthermore, we analyzed whether lipid profiles differ between CLA and CSA and found that CSA carry significantly greater levels of various SMs, CERs, and HCERs compared to CLA (Figures S3D and S3E). Overall, our data indicates that CLA, ILA, CSA, and ISA carry different lipid cargoes specific to their origin.

Adipomes derived from AT of *T. cruzi*-infected and uninfected mice differently regulate immunometabolic signaling in macrophages and alter macrophage polarization

We have demonstrated a significant regulatory impact of cultured adipocyte-derived adipomes on gene expression in macrophages (Figure 1F). Additionally, our research has revealed that WAT-derived adipomes carry specific lipid cargoes unique to infection status and adipome type (Figure 3). These findings suggest that adipomes derived from uninfected and infected mice may differentially influence macrophages, which play a vital role in pathogen and dead cell clearance. For instance, adipomes enriched with ceramides (ILA) can induce macrophage M1 polarization,[42] while those enriched with triacylglycerols (ISA) may cause macrophage mitochondrial oxidative stress.[43] Thus, we explored the regulatory effects of WAT-derived adipomes in macrophages *ex vivo*. To assess the impacts of adipomes from different sources (CLA, ILA, CSA, and ISA) on macrophages, we treated RAW 264.7 macrophages with adipomes at a 1:1 cell-to-adipome ratio for 48 h. Subsequently, we performed qPCR analysis of both treated and untreated macrophages using a custom-designed RT2 Profiler qPCR array (Qiagen). This array includes genes associated with adipogenesis (*Adipoq, Pparg, Fabp4*), lipogenesis (*Cebpa, Srebf1, Fas*), cellular metabolism-specific signaling molecules (*Slc2a4, Sphk1, Sgk2, Cpt1b, Slc27a4, Adra1a, Adra1b, Adipor1, Adipor2, and Insr*), as well as markers of inflammatory and immune responses (*Adgre1, Ccl5, Cxcl10, Ifng, Il1a, Il1b, Il10, Il17a, Il2, Il4, Il6, Tnfa, Tlr2, Tlr4, Tlr9, Ccr5, Ccr6, Cd80, Cxcr3, Cxcr5, Foxp3, Cd40, Cd86, Myd88*, and *Nfkb1*) (Figure S4A).
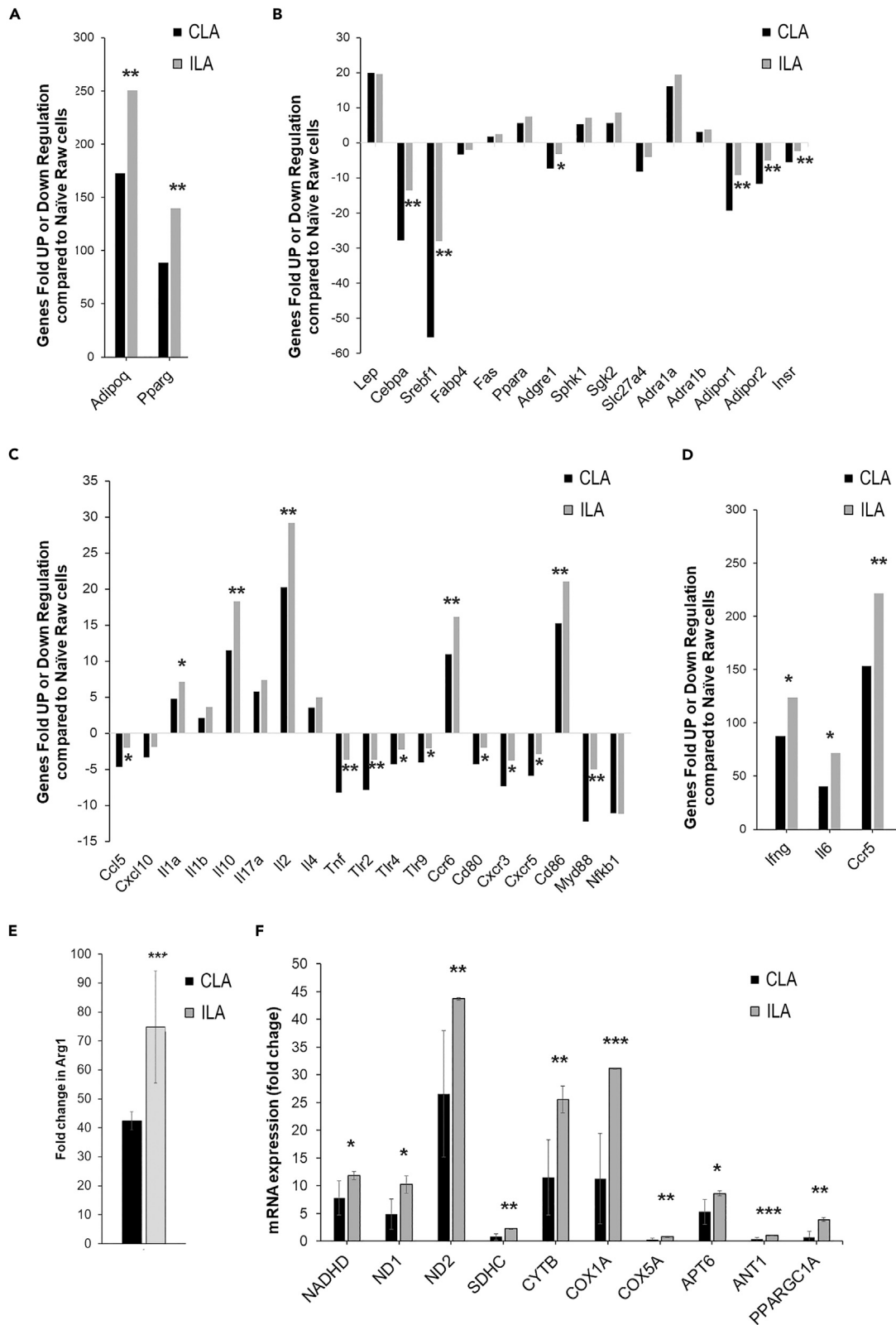
Figure 4. Infected L-adipomes alter immunometabolic signaling and macrophage polarization

(A–D) Changes in the expression of genes involved in adipogenesis (A), lipid metabolism (B), and immune and inflammatory signaling (C and D) based on mRNA fold change values (normalized to *Hprt*) in macrophages treated with CLA and ILA for 48 h as demonstrated by custom RT2 Profiler qPCR array analysis. Fold change was calculated using Qiagen data analysis spreadsheet.

(E and F) Fold change expression of *Arg1* mRNA transcript (E) and mRNA levels of genes involved in mitochondrial oxidative phosphorylation (F) (normalized to *Gapdh*) in macrophages treated with CLA and ILA for 48 h as demonstrated by qPCR analysis (n = 3). Data are represented as mean ± SEM. (*$p < 0.05$, **$p \leq 0.01$, and ***$p \leq 0.001$).

First, we compared the gene expression between macrophages treated with L-adipomes (CLA or ILA-treated groups) and naive macrophages. We observed a significant upregulation of Adipoq (adiponectin) and Pparg in macrophages treated with CLA or ILA compared to naive cells (Figure 4A). Additionally, with the exception of *Cebpa, Srebf1, Fabp4, Slc27a4*, adiponectin receptors *Adipor1* and *Adipor2*, and *Insr*, all other genes involved in metabolic signaling exhibited significant increases in macrophages treated with CLA/ILA compared to naive cells (Figure 4B). Moreover, the mRNA levels of pro-inflammatory signaling molecules such as *Tnfα, Tlr2, Tlr4, Tlr9*, and *Myd88* were significantly decreased, while the levels of anti-inflammatory signaling molecule *Il10* were significantly increased in macrophages treated with CLA/ILA compared to naive macrophages (Figure 4C). Furthermore, qPCR data demonstrated significantly higher levels of *Ifng, Il6*, and *Ccr5* in macrophages treated with CLA/ILA (Figure 4D). It is noteworthy that even though the levels of *Ifng* and *Il6* were significantly upregulated in adipome-treated macrophages, the pro-inflammatory cytokine *Tnfa* was significantly downregulated compared to naive macrophages, suggesting a possible shift in macrophage polarization toward M2.

As part of our investigation into macrophage polarization, we examined the mRNA levels of Arginase (*Arg1*), which serves as a marker of M2 macrophages and plays a key role in macrophage activation and polarization. The results revealed a significant increase in *Arg1* levels in macrophages treated with adipomes compared to naive macrophages (Figure S5A). Moreover, when comparing CLA and ILA treated cells, we observed significantly higher levels of *Arg1* in the ILA-treated cells (Figure 4E). Interestingly, both CSA and ISA-treated macrophages showed significantly reduced levels of *Arg1* compared to CLA and ILA-treated cells, respectively (Figure S5B). These findings indicate that adipomes regulate metabolic and immune signaling in macrophages by inducing adiponectin expression, inhibiting *Nfkb-Tnfa* activation, and promoting M2 polarization. Additionally, these data suggest that ILA significantly upregulates adipogenic genes, *Il10*, and *Arg1* in macrophages compared to CLA, CSA, and ISA. This finding may have implications for macrophage activation in infected mice and the clearance of parasites from infected organs.

Quantitative analysis revealed significant differences between macrophages treated with adipomes and untreated macrophages (Figure S4B). The genes most significantly and highly upregulated in adipome-treated macrophages compared to naive macrophages were *Adipoq, Pparg, Ifng, Il6*, and *Ccr5* and downregulated were *Nfkb, Tnfa, Cebpa, Srebp1, Adipor1, Adipor2* and *Insr*, indicating that adipomes regulate immunometabolic genes in macrophages. Furthermore, the origin of adipomes (CLA, ILA, CSA, and ISA) was also associated with notable differences in the levels of specific genes (Tables S3 and S4). For example, in the comparison between ISA- and CSA-treated macrophages, the mRNA levels of *Il4*, and *Ccr5* (anti-inflammatory signaling) were significantly downregulated in ISA-treated macrophages compared to CSA-treated macrophages, suggesting that infection generated ISA promotes pro-inflammatory signaling.

The upregulation of adipogenic genes, such as *Adipoq* and *Pparg*, and the downregulation of other genes involved in glucose and lipid metabolism, such as *Cebpa, Srebf1*, and *Slc27a4*, in adipome-treated macrophages could potentially impact energy pathways and differentially influence mitochondrial functions relative to naive macrophages. To explore this further, we analyzed the mRNA levels of mitochondrial genes associated with oxidative phosphorylation, including *Nadhd, Nd1, Nd2, Sdhc, Cytb, Cox1a, Cox5a, Apt6, Ant1*, and *Ppargc1a*. Our qPCR analysis revealed a significant increase in *Nadhd, Nd1, Nd2, Cytb, Cox1a*, and *Apt6* in all the adipome-treated groups compared to naive macrophages (Figure S5C). Furthermore, when we compared the levels of these genes between CLA- and ILA-treated cells, we found that all these genes were significantly increased in ILA-treated macrophages compared to CLA-treated macrophages (Figure 4F). Additionally, the levels of *Cox5a* and *Ant1* were significantly decreased in CSA- and ISA-treated macrophages compared to naive macrophages (Figure 4F). Moreover, between ILA- and ISA-treated macrophages, the above-mentioned genes were significantly upregulated in macrophages treated with ILA compared to ISA, suggesting that ILA may highly regulate mitochondrial functioning genes. These findings indicate significant alterations in mitochondrial gene expression among macrophages treated with adipomes of different origin (Figures 4F and S5D–S5F). These results suggest that, depending on the state of AT (e.g., infected vs. non-infected), AT-derived adipomes can influence mitochondrial gene expression differently in macrophages, potentially impacting their cellular energy metabolism and functions.

Adipomes upregulate lipogenic, mitochondrial and inflammatory genes in cardiomyocytes

To investigate whether adipomes can also regulate non-phagocytic cells in the heart, we treated murine primary cardiomyocytes with adipomes (1:1) derived from different sources (CLA, ILA, CSA, and ISA) for 48 h. Subsequently, we analyzed the mRNA expression of various genes, including Adipoq and adiponectin receptors (*Adipor1* and *Adipor2*), lipolytic signaling (β-AR, beta-Adrenergic Receptor, *Adrb2*), lipogenic genes (*Srebp1a* and *Srebp1c*), mitochondrial signaling (*Nadhd, Nd1, Nd2, Sdhc, Cytb, Cox1a, Cox5a, Apt6, Ant1*, and *Ppargc1a*), and inflammatory genes (*Tnfa* and *Ifng*) by qPCR.

qPCR analysis revealed that adipomes from all the groups significantly upregulated the expression of *Adrb2, Tnfa, Srebp1a*, and *Nd2* in cardiomyocytes compared to untreated cells (Figures 5A–5C). However, ILA treatment significantly altered most of the genes tested, with the exception of *Adipoq, Srebp2, Sdhc*, and *Cytb* (Figures 5A–5C). In the comparison between ILA- and CLA-treated macrophages, the levels of *Pparg* were significantly upregulated in ILA-treated cells compared to CLA-treated cells (Figure S6A). qPCR demonstrated a substantial
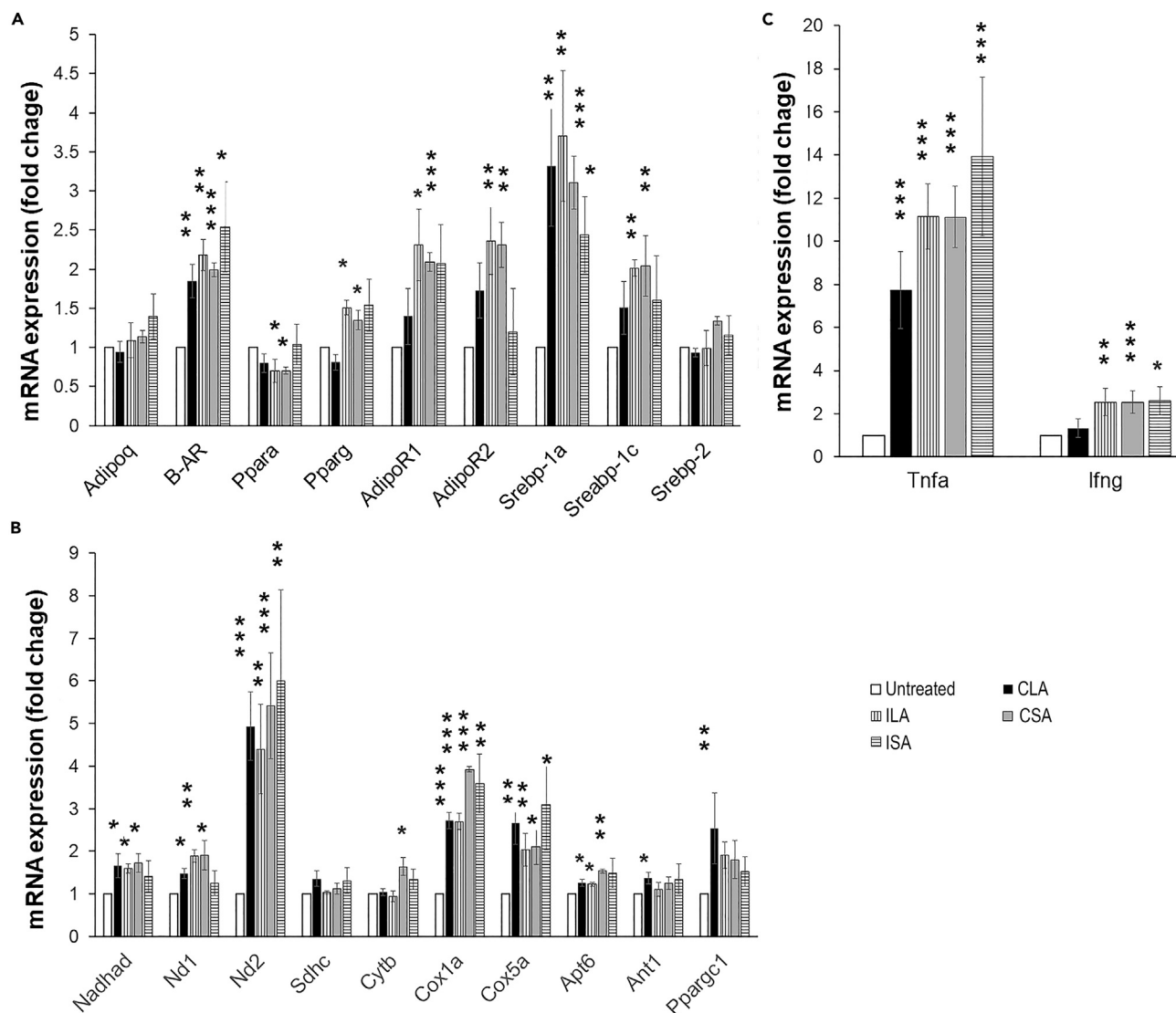
Figure 5. Adipomes play a major regulatory role in cardiomyocytes functioning

(A–C) Fold change in mRNA transcript levels of genes involved in adipogenic and lipogenic signaling (A), mitochondrial oxidative phosphorylation (B), and inflammatory signaling (C) (normalized to *Gapdh*) in murine primary cardiomyocytes treated with CLA, ILA, CSA, or ISA for 48 h and compared to untreated cardiomyocytes as demonstrated by qPCR analysis (n = 3). All adipome-treated groups (CLA, ILA, CSA, and ISA) were compared to untreated groups. Data are represented as mean ± SEM. (*$p < 0.05$, **$p \leq 0.01$, and ***$p \leq 0.001$).

upregulation of adiponectin receptors (*Adipor1* and *Adipor2*) in adipome-treated cardiomyocytes, while the levels of adiponectin remained unchanged compared to untreated cardiomyocytes (Figure 5A). Specifically, the levels of *Adipor1* and *Adipor2* were significantly higher in cardiomyocytes treated with ILA and CSA compared to those treated with CLA. Adipome treatment also led to a significant increase in the expression of *Adrb2* and *Srebp1a* genes in cardiomyocytes, suggesting that adipomes alter lipid metabolism. Furthermore, *Srebp1c* was significantly increased in ILA and not in CLA compared to untreated cardiomyocytes.

This increased lipogenic signaling and stimulation of lipolysis through β-AR appears to upregulate mitochondrial functions.[44,45] Among the analyzed genes encoding mitochondrial proteins, adipome treatment (regardless of origin) significantly altered the levels of *Nd2*, *Cox1a,* and *Cox5a* genes in cardiomyocytes (Figure 5B). The levels of the *Nd1* gene were significantly upregulated in cells treated with ILA and CSA compared to untreated cells. Increased mitochondrial oxidative phosphorylation leads to an increase in reactive oxygen species production, which in turn influences TNFα in a positive feedback loop.[46] Indeed, our data also showed a significant increase in the mRNA levels of *Tnfa* in adipome-treated cardiomyocytes compared to untreated cells (Figure 5C). Additionally, qPCR demonstrated an upregulation of *Ifng* levels in ILA-, CSA-, and ISA-treated cells, but not in CLA-treated cells, compared to untreated cardiomyocytes (Figure 5C). These findings suggest that adipomes enhance lipogenic signaling in cardiomyocytes, leading to increased mitochondrial oxidative
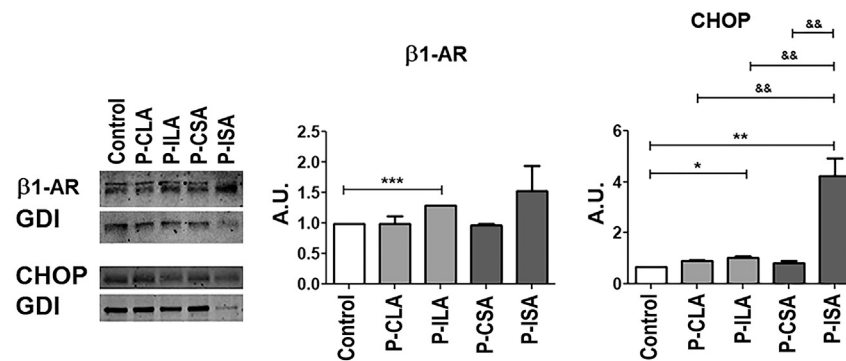
Figure 6. Circulatory adipomes induce ER stress in cardiomyocytes

Immunoblot analysis of β1-AR and CHOP expression in murine primary cardiomyocytes treated with plasma-derived adipomes (P-CLA, P-ILA, P-CSA, and P-ISA) and naive cells (n = 3/group). Bar graph values were derived from densitometry analysis and by normalizing target protein expression to GDI. The "&" symbol denotes significance calculated between different adipome-treated groups. Data are represented as mean ± SEM. (*p < 0.05, **p ≤ 0.01, and ***p ≤ 0.001).

phosphorylation and inflammatory signaling. Notably, ILA treatment further upregulated lipogenic signaling compared to CLA via the upregulation of *Pparg* (Figure S6A). Interestingly, no significant difference in macrophage gene regulation was observed between ILA and ISA-treated macrophages, whereas CSA treatment significantly increased lipogenic signaling and mitochondrial oxidative signaling compared to CLA, suggesting that uninfected WAT-derived L- and S- adipomes differently regulate macrophages. Overall, our data demonstrate that CLA, ILA, CSA, and ISA regulate both macrophages and cardiomyocytes, and that they differentially alter adipogenic, lipogenic, mitochondrial oxidative, and inflammatory signaling in these target cells.

Plasma-derived infection-associated adipomes (L- and S-) induce endoplasmic reticulum stress in primary cardiomyocytes

Our qPCR analysis revealed that adipomes derived from AT regulate the mRNA expression of β-AR, a marker of arrhythmic cardiomyopathy (Figure 5). Thus, we also analyzed the protein levels of β-AR in cardiomyocytes exposed to adipomes (at a cell-to-adipome ratio of 1:25 for 48h) by immunoblotting analysis. Notably, the levels of β-AR were significantly higher in cardiomyocytes treated with plasma-derived L-adipomes isolated from infected mice compared to naive cardiomyocytes (Figures 6 and S1A). β-AR stimulation is known to induce endoplasmic reticulum (ER) stress in cardiomyocytes.[47] Consequently, we analyzed the protein levels of CHOP, an ER stress marker, and discovered that both L- and S- adipomes specifically from infected mice plasma significantly increased the levels of CHOP in cardiomyocytes compared to naive cells. This data indicates that plasma-derived L-adipomes from infected mice regulate β-AR signaling, which is linked to lipid metabolism and arrhythmias in cardiac cells.
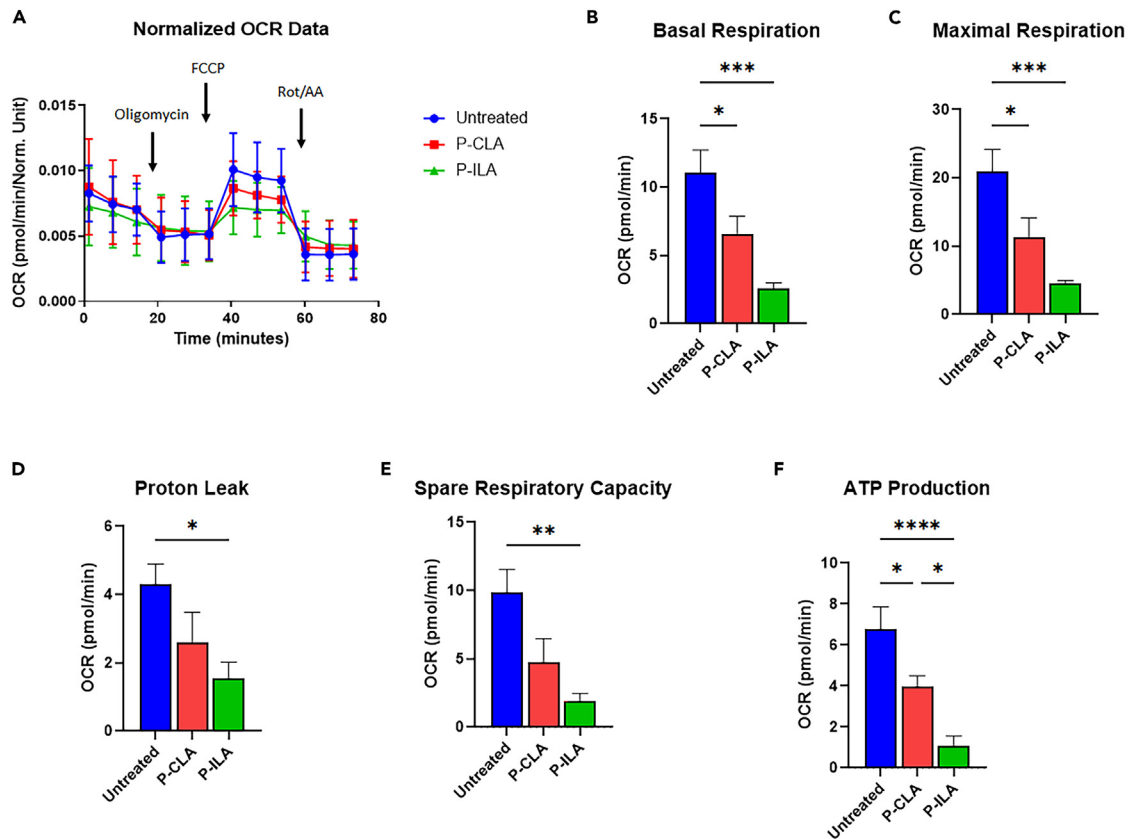
P-ILA induce mitochondrial dysfunction in primary cardiomyocytes

Increased lipogenic signaling can strain mitochondrial functions, potentially leading to mitochondrial dysfunction and arrhythmias.[48–50] To investigate whether PILA-induced arrhythmogenic β-AR signaling in cardiomyocytes is attributable to heightened lipogenic signaling-associated mitochondrial dysfunction, we assessed mitochondrial bioenergetics by Seahorse XFe96 analyzer, using the Seahorse XF Cell Mito Stress Test kit as described in the STAR Methods section. We measured changes in oxygen consumption rate (OCR) in P-ILA-treated mouse primary cardiomyocytes, revealing significantly reduced basal and maximal respiration, as well as ATP production, in P-ILA-treated cardiomyocytes compared to both naive and P-CLA-treated cells (Figure 7). These data suggest that P-ILA induces mitochondrial dysfunction and exacerbates arrhythmias.

P-ILA elevate the risk for cardiomyopathy in wild-type mice

We previously demonstrated that inducing adipocyte apoptosis increases the risk of cardiomyopathy in *T. cruzi*-infected mice during both the acute and chronic stages of infection.[11] In this study, we further showed that AT from infected mice releases higher levels of large adipomes (L-adipomes), and their lipid contents differ compared to those of uninfected mice. To investigate whether L-adipomes exist in circulation and can regulate the myocardium during infection, we isolated L-adipomes from the plasma of *T. cruzi*-infected (20 DPI) and wild-type C57BL/6J mice. Plasma-derived infection-associated large adipomes (P-ILA) from infected mice displayed a size range of 300–800 nm, as analyzed by Spectradyne (Figures S1A and S7A). Ultrasound-guided intramyocardial adipome injection was performed twice a week, with PBS-injected wild-type C57BL/6J mice serving as controls. Cardiac ultrasound analysis one week after the initial treatment revealed significant alterations in cardiac morphology in mice treated with P-ILA compared to the control group, including an increased left-ventricle internal diameter (LVID), right-ventricle internal diameter (RVID), and septal wall thickness at diastole (d) (Table 2). Mice treated with P-ILA also exhibited a greater left-ventricle ejection fraction (EF) compared to mice treated with the vehicle (64.383 ± 4.040 vs. 42.817 ± 3.325; Table 2). It is important to note that these measurements were carried out in sedated mice and, as reported previously,[51] sedation reduced the normal EF level from approximately 65% to approximately 35% in C57BL/6J mice. Notably, increased EF levels have been observed in murine models of

Figure 7. P-ILA cause mitochondrial dysfunction in primary cardiomyocytes

(A) Seahorse Mito Stress assay showing the oxygen consumption rate (OCR) from plasma-adipome treated (P-CLA and P-ILA) and untreated mouse cardiomyocytes ($n \geq 6$). Data normalized to nuclear content by staining and fluorescence cell counting.

(B–F) Representative graphs depicting the different mitochondrial respiration parameters evaluated, such as basal respiration (B), maximal respiration (C), proton leak (D), spare respiratory capacity (E), and ATP production (F). Data are represented as mean $\pm$ SEM. (*$p < 0.05$, **$p \leq 0.01$, ***$p \leq 0.001$, and ***$p \leq 0.0001$).

cardiac hypertrophy[52] and according to the American Heart Association, an EF measurement higher than 75% could indicate a heart condition such as hypertrophic cardiomyopathy in patients.[53] Thus, the significantly increased EF levels in P-ILA-treated mice compared to vehicle-treated mice suggest that P-ILA treatment may induce a hypertrophic cardiomyopathy phenotype in wild-type C57BL/6J mice.

Alteration of inflammatory and metabolic signaling in the heart by P-ILA increases cardiomyopathy risk in post-acute Chagas mouse model

The data presented above suggested that P-ILA treatment may exacerbate cardiac pathology in CD mice. To investigate whether P-ILA affect cardiac pathology and whether they may exacerbate the cardiomyopathic phenotype during chronic infection, we replicated the *in vivo* experiment using both uninfected and post-acute *T. cruzi*-infected (35 DPI) C57BL/6J mice, as outlined in the STAR Methods section. Both uninfected and *T. cruzi*-infected mice were treated with PBS to serve as appropriate controls. Ten days after the initial treatment, the mice were sacrificed, and their hearts were harvested for histological and biochemical analysis to assess the impact of adipome treatment on the myocardium.

The H&E sections of the hearts revealed an increased infiltration of immune cells in the hearts of both P-ILA-treated uninfected and infected mice, specifically in the epicardium and right ventricles (Figures S7B and S7C). An analysis assessing the impact of adipome treatment on fibrosis showed no significant differences in fibrosis levels between mice that received adipome treatment and those that did not, in both uninfected and infected groups (Figure S7D). However, fibrosis levels notably increased in the infected groups (both P-ILA-treated and untreated) compared to uninfected groups. This was evident in the results of Picrosirius Red Polarization (PSRP) staining (Figure S7D). Considering the regulatory influence of adipomes on the expression of TNFA in cultured macrophages and primary cardiomyocytes *in vitro* (Figures 4 and 5), we also investigated their effect on TNFA protein expression in the myocardium through immunohistochemical (IHC) analysis. We found that treatment with P-ILA elevated the levels of TNFA in the myocardium compared to treatment with the vehicle in uninfected mice but not in infected mice. However, the levels of TNFA were significantly increased in the myocardium of infected mice compared to uninfected mice (Figure S7E). We further investigated the protein levels of inflammatory markers, namely TNFA, IFNG, and IL6, in the heart

Table 2. Cardiac ultrasound analysis (M mode) showing altered LVID, RVID and other parameters including EF in mice treated with P-ILA compared to control mice

ECG Measurement	Vehicle	P-ILA
LVID (d) mm	3.695 ± 0.083	3.999 ± 0.095**
LVID (s) mm	2.643 ± 0.057	2.675 ± 0.125
LVPW (d) mm	4.950 ± 0.233	5.330 ± 0.070*
LVPW (s) mm	4.055 ± 0.385	4.265 ± 0.095
RVID (d) mm	0.976 ± 0.142	1.462 ± 0.002**
RVID (s) mm	0.638 ± 0.087	0.764 ± 0.024
RVED (d) mm	1.503 ± 0.181	1.932 ± 0.059*
RVED (s) mm	1.275 ± 0.094	1.492 ± 0.052*
Septal Wall (d) mm	0.471 ± 0.018	0.599 ± 0.016***
Septal Wall (s) mm	0.325 ± 0.006	0.398 ± 0.010***
LVEF	42.817 ± 3.325	64.383 ± 4.040**

ECG, electrocardiography; LVID, left ventricular internal diameter; LVPW, left ventricular posterior wall; RVID, right ventricular internal diameter; RVED, right ventricular end-diastolic area; LVEF, left ventricular ejection fraction; d, diastole; s, systole; P-ILA, plasma-derived infection-associated L-adipomes. *$p \leq 0.05$, **$p \leq 0.01$ compared to control mice (vehicle-treated).

lysates through immunoblotting analysis. The analysis revealed significantly higher levels of TNFA and IL6 in P-ILA-treated uninfected mice and only IL6 in P-ILA-treated-infected mice compared to their respective vehicle-treated groups (Figure 8A). Immunoblotting analysis of F4/80 in heart lysates demonstrated that P-ILA treatment also significantly increased the infiltration of macrophages into the hearts (Figure 8A). Together, these data suggest that P-ILA treatment induces macrophage infiltration in the hearts of both uninfected and infected mice and increases TNFA only in uninfected mice but does not alter M1-cytokine markers such as TNFA and IFNG in infected mice.

In addition to its key role during inflammation, the pleiotropic cytokine IL6 is involved in lipid metabolism in both humans and rodents by stimulating lipid hydrolysis and mitochondrial β-oxidation to prevent cardiac lipotoxicity.[54,55] Therefore, we analyzed the levels of SREBP1 and perilipin, markers of lipogenesis and lipid droplets, respectively, and found that the levels of both these proteins significantly increased in the hearts of P-ILA-treated uninfected mice but not in infected mice compared to their respective vehicle-treated groups (Figure 8B). This data mirrors our *in vitro* observations where adipome treatment significantly increased lipogenic genes in primary uninfected cardiomyocytes (Figure 8B). Interestingly, we noted that the levels of both SREBP1 and perilipin were significantly decreased in vehicle-treated infected mice compared to vehicle-treated uninfected mice, indicating that acute infection reduces lipid levels in the hearts, either inhibiting lipogenesis or by increasing lipid utilization in the heart. To test whether P-ILA treatment increases cardiac lipid hydrolysis and oxidation, we analyzed the levels of phospho-perilipin (p-Perilipin) and PPARα, markers of lipid hydrolysis and lipid oxidation, respectively.[56,57] We found that the levels of p-Perilipin and PPARα significantly increased in the hearts of infected mice compared to uninfected groups, and the treatment with P-ILA further significantly increased the levels of both markers in infected mice (Figure 8B). These data suggest that increased lipid hydrolysis may elevate mitochondrial β-oxidation.[58]

Our *in vitro* data indicated that adipomes regulate mitochondrial genes involved in oxidative phosphorylation. To further explore these findings *in vivo*, we analyzed the levels of markers of mitochondrial oxidative phosphorylation, such as SDHA, Cytochrome *c*, COX IV, and HSP60 (Figure 8C). P-ILA treatment significantly increased the levels of SDHA and HSP60 only in uninfected mice (but not in infected mice) compared to vehicle treatment (Figure 8C). Interestingly, P-ILA treatment significantly reduced the levels of cytochrome *c* in both uninfected and infected mice and significantly reduced COX IV only in the infected mice compared to vehicle treatment. These data suggest that P-ILA treatment affects mitochondrial oxidative phosphorylation and may have especially deleterious effects on the hearts of infected mice, where lipid hydrolysis is significantly increased compared to uninfected mice.

P-ILA induces ER stress in the heart, elevating cardiomyopathy risk in post-acute Chagas mice

Previously, we demonstrated that the onset of cardiomyopathy in *T. cruzi*-infected mice, induced by adipocyte apoptosis, is associated with decreased mitochondrial oxidation (cytochrome *c* levels) and increased ER stress.[11] Therefore, we analyzed the levels of ER stress markers – Binding immunoglobulin protein (BiP), protein kinase R- (eIF2α), protein disulfide isomerase (PDI) and C/EBP homologous protein (CHOP) – in heart lysates. Our findings indicate a significant increase in the levels of BiP, PDI, and phospho-eIF2α in the hearts of P-ILA-treated-infected mice and only BiP in the hearts of P-ILA-treated uninfected mice compared to the respective vehicle-treated groups (Figure 8D). Elevated BiP and phospho-eIF2α levels are indicative of increased ER stress.[59] ER stress, in turn, is known to raise CHOP levels, which can activate apoptosis.[60,61] Indeed, immunoblotting analysis data revealed an increase in both CHOP and cleaved caspase (an apoptosis marker), but not BNIP3 (a necrosis marker), in P-ILA-treated-infected mice (Figures 8D and 8E), indicating that P-ILA induces ER stress and apoptosis while concurrently diminishing mitochondrial functions in the hearts in infected mice. However, in uninfected mice, although P-ILA treatment increased BiP and CHOP levels (but not phospho-eIF2α), the levels of cleaved caspase were not increased compared to vehicle treatment.
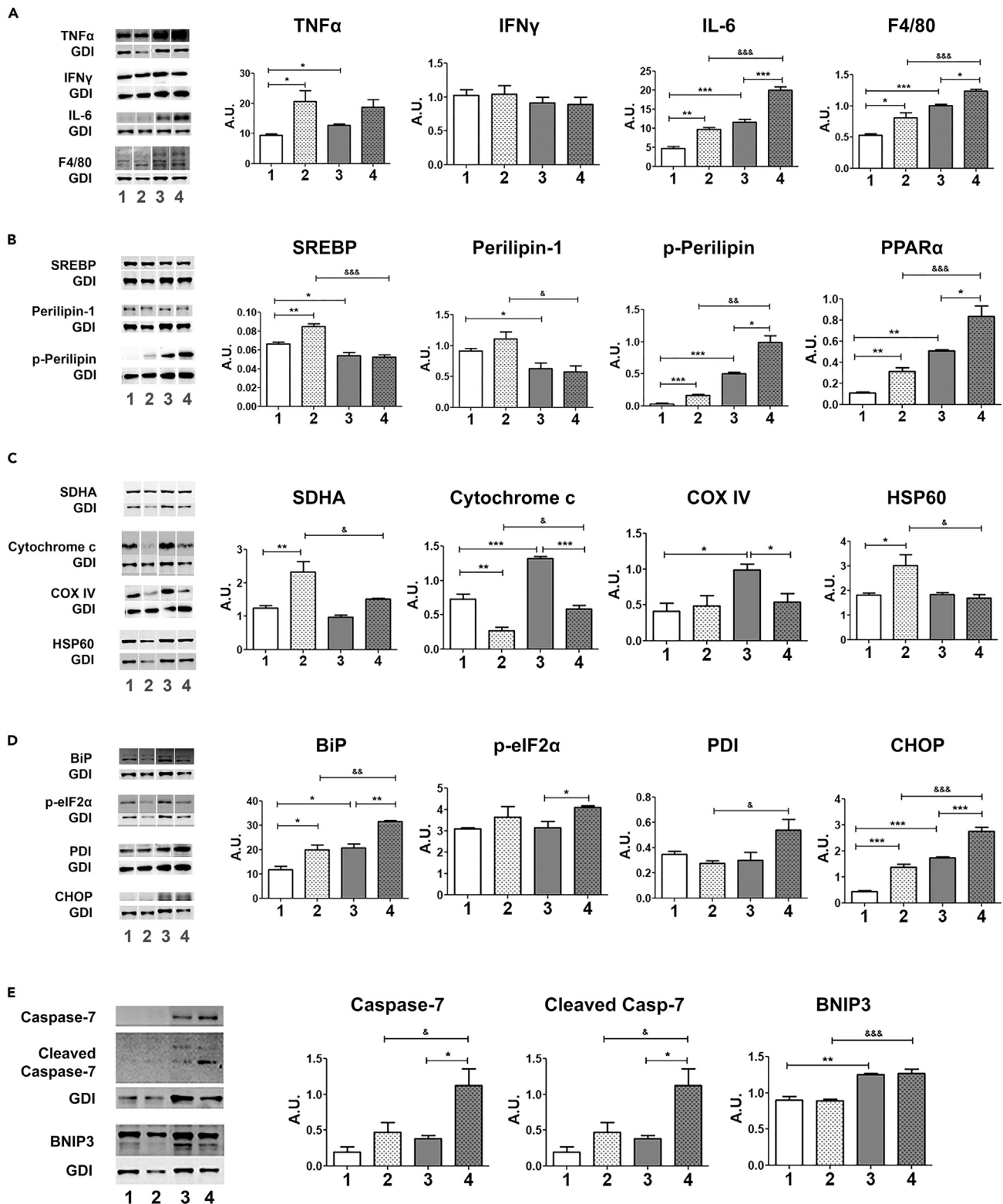
Figure 8. P-ILA elevate the risk for cardiomyopathy in murine CD model during post-acute phase

(A–E) Immunoblot analysis of inflammation (TNFα, IFNγ, IL6), immune cell infiltration (F4/80), lipogenesis (SREBP1), lipid droplet formation (Perilipin-1), lipid hydrolysis (phospho-Perilipin), lipid oxidation (PPARα), mitochondrial oxidative phosphorylation (SDHA, Cytochrome *c*, COX IV, HSP60), ER stress (BiP,

This could be due to increased HSP60 levels in the hearts of P-ILA-treated uninfected mice, which can promote cell survival and inflammation as indicated by increased TNFα levels in the hearts.[62,63] Our data indicates that in uninfected mice, P-ILA treatment induces ER stress associated with lipogenesis, impaired mitochondrial oxidative phosphorylation, and elevated proinflammatory TNFα signaling, whereas in infected mice, P-ILA treatment induces ER stress associated with lipid hydrolysis, impaired mitochondrial oxidative phosphorylation, and elevated apoptosis signaling.

Next, drawing on previous reports,[5,11,64,65] we analyzed specific markers of cardiomyopathy using heart lysates and heart sections to further clarify the role of P-ILA in regulating CCM. Chagas heart disease is considered an arrhythmogenic cardiomyopathy characterized by atrial and ventricular arrhythmias and a wide variety of abnormalities of the conduction system.[11] Beta-adrenergic receptors in the heart play a crucial role in regulating heart rate and contractility,[66] and overactivation of beta-adrenergic receptors can potentially lead to arrhythmias.[67] CD is also known to increase the levels of β1-AR and ANP in the hearts of experimental animals and patients.[64,65] Murine CD models with cardiomyopathy display elevated levels of adiponectin in the hearts.[11] Immunoblotting analysis of heart lysates demonstrated that P-ILA treatment significantly increases the levels of adiponectin and β1-AR in the hearts of mice compared to vehicle treatment, both in infected and uninfected mice (Figure 9A). IHC analysis further revealed elevated ANP levels in the hearts of P-ILA-treated mice compared to vehicle-treated mice (Figure 9B), suggesting that P-ILA treatment induces cardiomyopathy in uninfected mice and exacerbates the severity of cardiomyopathy in post-Chagas-infected mice.

P-ILA do not carry *T. cruzi* in their cargo

To investigate whether the observed effects in the hearts of P-ILA-treated mice were due to P-ILA-associated *T. cruzi*, we conducted qPCR analysis of *T. cruzi*-specific gene in heart extracts, as previously demonstrated.[17] Our results revealed no trace of parasites in the hearts of both
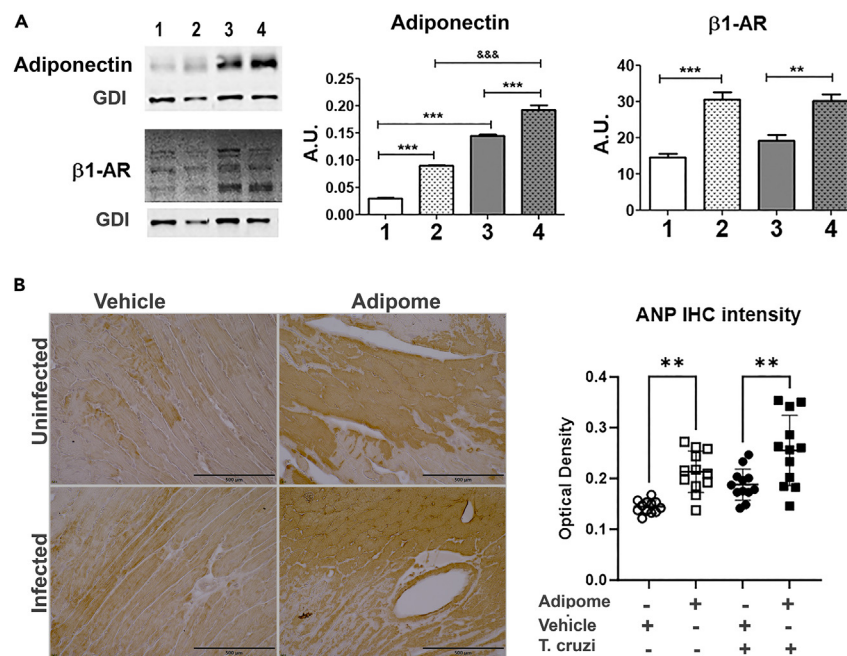
Figure 9. Intracardiac P-ILA treatment increases cardiac adiponectin (APN) and Atrial natriuretic peptide (ANP) in murine CD model

(A) Immunoblot analysis of adiponectin and β1-AR expression in heart lysates of uninfected and post-acute *T. cruzi*-infected mice treated with intracardiac injections of either P-ILA or vehicle. Bar graph values were derived from densitometry analysis and by normalizing target protein expression to GDI. Lanes: 1, uninfected vehicle-injected; 2, uninfected P-ILA-injected; 3, *T. cruzi*-infected vehicle-injected; and 4, *T. cruzi*-infected P-ILA-injected murine heart tissue lysate. The "&" symbol indicates significance calculated between uninfected and *T. cruzi*-infected P-ILA injections.

(B) Representative immunohistochemistry (IHC) images of vehicle- and P-ILA-injected heart tissue from uninfected and *T. cruzi*-infected mice showing ANP immunostaining visualized with DAB and counterstained with hematoxylin. Dot plot shows staining intensity in O.D. (mean gray value) obtained by color deconvolution analysis. Data are represented as mean ± SEM. (**$p \leq 0.01$, and ***$p \leq 0.001$).

P-ILA-treated and untreated post-infected mice, and no detectable parasites in P-ILA-treated uninfected mice (Figure S8). The near absence of parasite genetic material in post-infected mice (45 DPI) can be attributed to the use of a low parasite load (10^3) in the initial infection, which typically diminishes significantly in the hearts following acute infection.[17] The lack of a significant increase in parasite genetic material in P-ILA-treated post-infected and uninfected mice suggests that adipomes do not harbor parasites. To reinforce this finding, we conducted qPCR analysis of *T. cruzi* in P-ILA-treated cultured cardiomyocytes (1:20 ratio, 48 h), revealing the absence of parasites in treated cells (Figure S8). Furthermore, the size of the parasite ranges between 2 and 6μm, which is significantly larger than that of L-adipomes (Figure S7A), making it unlikely that adipomes harbor parasites.

Overall, our *in vivo* data demonstrate that intracardiac P-ILA treatment increases the infiltration of macrophages, elevates β-AR, adipogenic and IL6 signaling, impairs mitochondrial oxidative phosphorylation, and induces ER stress in the myocardium. In addition, P-ILA regulate lipogenesis and TNFα signaling in the hearts of uninfected mice and lipid hydrolysis and apoptosis signaling in infected mice, leading to hypertrophied cardiomyopathy and exacerbating cardiac pathology in uninfected and post-acute CD mice, respectively.

DISCUSSION

Chagas cardiomyopathy, which typically develops after several years or decades in approximately 30% of *T. cruzi*-infected patients, manifests a broad spectrum of cardiac abnormalities, ranging from ECG abnormalities to multi-ventricular dysfunction and heart failure. Interestingly, recent reports suggest that individuals in the acute phase can also progress to a chronic form of acute cardiomyopathy (ACM).[4] The progression to various forms of arrhythmogenic cardiac ailments in patients with CD is multifactorial.[5] Our prior data demonstrated a robust correlation between the loss of adipocytes and an elevated risk of cardiomyopathy in murine CD models.[17] Specifically, we illustrated that the reduction in body fat resulting from adipocyte apoptosis significantly intensifies the pathogenesis of cardiomyopathy in acute and early chronic CD mice.[11] These findings suggest that pathological adipocytes play a pivotal role in triggering cardiomyopathy during the acute and indeterminate stages of CD. However, the molecular mechanisms underlying adipocyte loss and its impact on the myocardium and its cells, such as cardiomyocytes, fibroblasts, and resident/infiltrated immune cells during infection, have remained unclear. In particular, whether adipocyte-derived adipomes can impact myocardial functioning and regulate cardiomyopathy has never been investigated. In this study, we aimed to address these questions using various *in vitro*, *ex vivo*, and *in vivo* models. Our findings reveal that: (i) *T. cruzi* infection induces adipocyte apoptosis and increases the release of adipomes that interact with various cell types, including cardiomyocytes and immune cells; (ii) Adipomes derived from AT of *T. cruzi*-infected mice carry distinct lipid cargoes compared to adipomes derived from uninfected mice and regulate the expression of immune and metabolic genes in cardiomyocytes, macrophages, and fibroblasts, which are the major cell populations found in the myocardium during infection; and (iii) Plasma-derived infection-associated large adipomes (P-ILA) increase the risk of the pathogenesis of cardiomyopathy by inducing ER stress and impaired mitochondrial oxidative phosphorylation, leading to inflammation-associated cardiomyopathy in uninfected mice and apoptosis-associated cardiomyopathy in post-acute CD mice. Specifically, our study showcased that P-ILA treatment triggers mitochondrial dysfunction and fosters arrhythmogenic β-AR signaling in primary cardiomyocytes. Furthermore, intracardiac P-ILA treatment was shown to induce the chronic manifestation of arrhythmic cardiomyopathy in post-acute Chagas disease (CD) mice. Another significant advancement in our study is the development of an innovative method for isolating adipomes directly from mouse plasma and AT, which enabled the subsequent characterization of their lipid contents and functional analysis.

CD has two stages: acute and chronic, the latter of which includes asymptomatic and symptomatic stages. Although the predominant clinical manifestations of CCM typically include dilated cardiomyopathy, congestive HF, arrhythmias, and cardio embolism, some patients also exhibit features reminiscent of hypertrophic cardiomyopathy.[4] In murine models of CD, the alteration of cardiac morphology presents differently in the acute and chronic stages of infection, mimicking the spectrum of CCM pathogenesis seen in patients. Mice with acute infection demonstrate enlarged right ventricular internal diameter (RVID) associated with LV wall thickening, resembling hypertrophic inflammatory cardiomyopathy.[68] Conversely, mice with late chronic infection exhibit increased RVID and LVID with wall thinning and decreased ejection fraction (EF%), resembling dilated cardiomyopathy with HF pre-symptoms.[11] We demonstrated that a loss of adipocytes influences the pathogenesis of cardiac CD using both acute and asymptomatic mice.[11] While in this study we utilized adipomes associated with acute *T. cruzi* infection to illustrate the impact of fat cell loss on hypertrophied cardiomyopathy development, these results represent a significant advancement in our general understanding of the intricate interplay among *T. cruzi* infection, adipocyte-derived adipomes, and myocardial function. It also offers valuable insights into the mechanisms likely disrupting immune and metabolic processes, thereby contributing to the pathogenesis of chronic cardiomyopathy in CD.

T. cruzi and other pathogens exploit AT to persist in a nutrient-rich environment and evade the immune system.[11,68–78] *T. cruzi* lacks cholesterol biosynthesis enzymes and depends on host cholesterol, making cholesterol-rich adipocytes a preferred host cell type for invasion.[19] In a previous *in vivo* study, we showed that *T. cruzi* infection induces oxidative stress and cell death in AT of infected mice.[11] However, previous studies did not determine whether apoptosis and/or necrosis of adipocytes were directly initiated by *T. cruzi* infection or indirectly triggered by immune cell-induced lipolysis in AT. In the current study, by utilizing human and murine cell lines of cultured adipocytes (in the absence of immune cells), we observed that the *T. cruzi* infection of cultured adipocytes induces apoptosis at 72 h post-infection. It is likely that after 96 h post-infection, *T. cruzi*-infected cultured adipocytes undergo necrotic cell death due to the egression of trypomastigotes after intracellular replication.[79] Adipocyte apoptosis may be a crucial phenomenon in Chagas infection during the asymptomatic stage. We have previously demonstrated that parasites persist in AT during the indeterminate and chronic stages of infection.[17] During the asymptomatic stage, parasites do not vigorously replicate and establish a symbiotic relationship with host cells.

However, the presence of the parasite in AT affects adipocyte physiology, leading to elevated lipolysis,[26] whereas impaired lipolysis is a potent trigger of adipocyte apoptosis.[80,81] Apoptosis is known to generate apoptotic bodies (membrane-bound EVs carrying valuable biological information) as well as other EVs, including microvesicles and exosomes.[31–33,82] Unlike EVs derived from other cell types, adipocyte-derived adipomes, including ApoBDs, contain large amounts of lipid metabolites alongside proteins and genetic material,[83,84] distinguishing them as a unique subset of EVs.

In the current study, we found compelling evidence that AT of acutely infected mice releases significantly higher levels (approximately 10-fold) of large EVs, including apoptotic bodies, compared to uninfected mice. Building on this discovery, we further isolated and characterized both large and small adipomes to analyze their functions in detail *ex vivo*. Most previous studies of adipocyte-derived EVs used EVs from cultured adipocytes or *ex vivo* cultured adipocytes.[21,22] In contrast, here we describe the first successful isolation of intact adipomes directly from mouse AT in its localized microenvironment using adiponectin as a surface marker, thus excluding EVs generated by non-adipocyte cells present in AT. We also identified distinct lipid cargoes specific to the origin and pathological condition of adipocytes. Infection-associated large adipomes (ILA) enriched with ceramides, sphingomyelins, and hexosylceramides have the potential to enhance the intracellular accumulation of sphingolipids and their derivatives in target cells, such as cardiomyocytes, fibroblasts and macrophages. This process could lead to heightened cardiotoxicity and the development of lipotoxic cardiomyopathy.[85–88] Moreover, excessive ceramides and triglycerides in macrophages can lead to macrophage apoptosis.[89] Intracellular lipid accumulation also affects mitochondrial functions in fibroblasts and skeletal muscle.[90–92] Our *ex vivo* data reveal that adipocyte-derived adipomes can regulate lipogenic/adipogenic, mitochondrial oxidative phosphorylation, and inflammatory signaling in target cells. Although our analysis showed subtle changes in mRNA expression between the target cells treated with different types of adipomes (CLA, ILA, CSA, and ISA), it is crucial to emphasize that the data underscore the regulatory impact of all adipomes on gene expression in target cells. Additionally, it is important to note that the ratio between adipomes and target cells, as well as the exposure time, may vary under physiological and pathological conditions *in vivo*. Moreover, while adipomes from uninfected mice exhibited similar effects, those from infected mice had a higher proportion of L-adipomes, resulting from adipocyte apoptosis during infection. This observation is highly relevant to the pathogenesis of cardiomyopathy in CD.

Our *in vitro*, *ex vivo*, and *in vivo* data reveal that adipomes regulate mitochondrial gene expression in macrophages, influencing the polarization of these cells. *Ex vivo* data demonstrates that adipome-treated macrophages exhibit increased mitochondrial gene expression, suggesting a shift toward oxidative phosphorylation, potentially promoting M2 polarization and anti-inflammatory signaling,[93] which may aid parasite persistence in the host. *In vivo* data showed no significant increase in the levels of pro-inflammatory cytokines (either TNFα or IFNγ) in the hearts of adipome-treated mice, although there was a significant increase in the infiltration of macrophages compared to vehicle-treated mice. These findings highlight the complex role of AT and adipomes in CD-related cardiac inflammation and remodeling. Contrary to our findings in fibroblast cells and macrophages, AT-derived adipomes from *T. cruzi*-infected mice did not affect adiponectin gene expression in cardiomyocytes. Instead, they increased the expression of lipogenic genes such as *Pparg*, *Srebp1a*, and *Srebp1c*. High levels of *Srebp1c* in cardiomyocytes could lead to increased mitochondrial oxidative phosphorylation, potentially causing lipotoxicity, oxidative stress and cell death.[94] Elevated oxidative phosphorylation produces ROS, inducing *Tnfa* expression to mitigate cellular toxicity.[46] Adipomes also induced the expression of inflammatory genes such as *Tnfa* and *Ifng* in cardiomyocytes. The endogenous production of *Tnfa* in cardiomyocytes promotes a predominantly pro-inflammatory response and results in apoptosis.[95,96]

Interestingly, our *ex vivo* and *in vivo* data reveal a different mechanism of lipotoxicity induced by adipome treatment in primary cardiomyocytes and the hearts of uninfected and infected mice. In primary cardiomyocytes, adipome treatment increased the expression of genes involved in adipogenic/lipogenic, mitochondrial oxidative, and inflammatory signaling that could lead to lipotoxicity and ROS-induced cell death. We observed some similarities in mRNA expression in primary cardiomyocytes to protein expression in P-ILA-treated hearts in uninfected mice, where the protein levels of lipogenic/adipogenic (perilipin, SREBP-1, adiponectin), mitochondrial oxidative phosphorylation (HSP60), and inflammatory (TNFα) signaling markers were significantly increased. In contrast, in the hearts of post-infected mice, P-ILA treatment increased lipid hydrolysis but significantly reduced the protein levels of mitochondrial oxidative phosphorylation function markers, potentially promoting apoptosis-induced cell death, as indicated by increased levels of cleaved caspase in the heart. It is essential to acknowledge, however, that the regulatory effects observed in cell lines or primary cells *in vitro* may differ from those observed in *in vivo* studies of whole animals. Such discrepancies could be due to various factors, including hormones, the presence of different immune cell populations, and metabolic regulators, all of which contribute to myocardial function.

Acute *T. cruzi* infection induces myocarditis with hypertrophy and fibrosis in both mice and humans. Cardiac remodeling, a crucial process during the asymptomatic phase of CD, involves the replacement of dead cardiomyocytes with fibroblasts and the resolution of pro-inflammatory immune responses, contributing to the remodeling phenomenon. However, instances of chronic cardiomyopathy have been observed in patients with acute CD,[4] and the cause for this early response is not fully understood. Our *in vivo* data suggests that adipomes can impact the myocardium through either paracrine or endocrine effects during any stage of infection, depending on the pathological status of AT. For example, adipomes released from pericardial fat might exert a paracrine effect, while circulating adipomes could exert an endocrine effect in the myocardium, directly interacting with cardiomyocytes and fibroblasts. This interaction could induce the infiltration of immune cells, inflammation, adipogenesis, mitochondrial dysfunction, and ER stress in the myocardium, leading to cardiomyopathy.[9–11] Cardiac fat plays a significant role in regulating metabolic functions and myocardial inflammation.[97,98] We have observed that pericardial fat disappears in acute *T. cruzi*-infected mice (Figure S2A), emphasizing its role in myocarditis and ventricular enlargement in CD. Adipocyte-specific hormone adiponectin

upregulates AMPK signaling in the myocardium, which is essential for cardiovascular functions,[99,100] but its overexpression in Chagas mice leads to adverse effects, such as increased adipogenesis, lipotoxicity, and mitochondrial dysfunction.[8] During the loss of healthy adipocytes, cardiac fat may not express sufficient hormones to regulate heart muscle cells, while adipomes from pathological adipocytes may influence gene expression in the heart. Our results demonstrate that adipome treatment increases adiponectin expression in fibroblasts and macrophages, which is further supported by the *in vivo* data showing that treatment with P-ILA elevates cardiac adiponectin levels (Figure 9A).

Our *in vivo* data demonstrate the functional role of P-ILA in elevating the risk and severity of the chronic form of cardiomyopathy in post-acute CD mice, associated with mechanisms involving lipid hydrolysis, impaired mitochondrial oxidative phosphorylation, ER stress, and apoptosis. In P-ILA-treated uninfected mice, the risk of cardiomyopathy is associated with mechanisms such as lipogenesis/adipogenesis and inflammation, similar to what we observed in adipome-treated primary cardiomyocytes. However, elevated β-AR signaling, and ER stress were observed in the hearts of both uninfected and infected mice treated with P-ILA. Previously, we demonstrated that the inhibition of ER stress improves cardiac morphology and functioning in chronic CD mice.[9] It has been shown that ER stress leads to apoptosis, inflammation, and cardiac hypertrophy.[101,102] Additionally, chronic β-AR stimulation induces ER stress.[47] It has also been shown that ER stress causes an increase in IL6.[103,104] Our data suggest that the increase in IL6 in the hearts is induced via ER stress in infected mice, which is exacerbated by P-ILA treatment. The chronic elevation of β1-AR in the heart is associated with cardiac hypertrophy and ventricular remodeling.[105–107] Our comprehensive analysis, spanning *in vitro*, *ex vivo*, and *in vivo* studies, underscores the regulatory impact of adipomes on β-AR signaling, and heightened β-AR signaling has been implicated as a potential precursor to arrhythmias.[67] Chagas heart disease, recognized as an arrhythmogenic cardiomyopathy, is characterized by atrial and ventricular arrhythmias, as well as a spectrum of conduction system abnormalities.[5] While arrhythmias commonly manifest in chronic patients with dilated cardiomyopathy, instances of hypertrophied cardiomyopathy have also been documented in Chagas disease.[108,109] Mitochondrial dysfunction promotes cardiac arrhythmias,[48–50] and our data demonstrate that P-ILA treatment in cardiomyocytes causes mitochondrial dysfunction and increases β-AR signaling. Our research further establishes elevated levels of ANP in the hearts of P-ILA-treated mice, adding another marker indicative of Chagas cardiomyopathy in both uninfected and infected mice. These compelling observations prompt the need for additional investigations to delve deeper into the functional role of adipomes in the intricate pathogenesis of chronic Chagas cardiomyopathy.

Our current study delves into the role of AT- and plasma-derived adipomes in the pathogenesis of cardiomyopathy. The myocardium can be regulated by exosomes derived from various cell types,[110,111] including exosomes produced by *T. cruzi*.[112] Studies have demonstrated that *T. cruzi*-derived EVs exert immunomodulatory effects with potential applications in CD treatment.[112,113] A noteworthy aspect of our study is the development of methods to isolate intact tissue-derived and circulating adipomes from mice. While several studies have used EVs derived from cultured or *ex vivo* adipocytes,[22,114,115] our research provides a valuable resource for isolating intact adipomes directly from organs and tissues to explore their functional role in various diseases. Further studies are essential to unravel the molecular mechanisms regulated by adipomes in the heart during the transition from chronic asymptomatic to symptomatic CD. Such investigations may uncover potential therapeutic targets to prevent the progression of dilated cardiomyopathy and heart failure.

Limitations of the study

The majority of our *ex vivo* data relies on gene expression analysis rather than protein assessment. Specifically, the gene expression data from cardiomyocytes treated with adipomes revealed an increased expression of genes associated with mitochondrial oxidative phosphorylation that could relate to oxidative stress-induced mitochondrial dysfunction. The intricate interplay between these regulatory effects and their ultimate impact on cardiomyopathy in primary cell culture needs to be further explored. Our study did not incorporate other infection models for comparison with *T. cruzi* infection. Therefore, we do not know whether the described findings are specific to *T. cruzi* infection. We did not assess whether adipomes carry *T. cruzi*-specific pathogen-associated molecular pattern molecules (PAMPs). While we utilized adipomes associated with acute *T. cruzi* infection to illustrate the impact of fat cell loss on hypertrophied cardiomyopathy development in this study, future studies are necessary to comprehensively evaluate how adipomes associated with chronic *T. cruzi* infection exert their regulatory influence on gene expression in target cells. Such investigations are crucial for a more nuanced understanding of the cellular and molecular events that contribute to the pathological processes associated with adipomes, particularly in the context of cardiomyopathy.

STAR★METHODS

Detailed methods are provided in the online version of this paper and include the following:

- KEY RESOURCES TABLE
- RESOURCE AVAILABILITY
  - Lead contact
  - Materials availability
  - Data and code availability
- EXPERIMENTAL MODEL AND STUDY PARTICIPANT DETAILS
  - Mammalian cell lines and parasites culturing
  - *T. cruzi* infection *in vitro*
  - Murine model of acute Chagas disease

- METHOD DETAILS
  - Adipome isolation and functional analysis
  - EXOCET assay
  - Immunofluorescence analysis
  - Nanoparticle Tracking
  - Transmission electron microscopy
  - Cardiac ultrasound imaging
  - Histological analysis
  - Immunoblotting analysis
  - RNA extraction and quantitative PCR
  - Lipidomics analysis
  - Magnetic resonance imaging (MRI)
  - Seahorse XF96 cell metabolic analysis
- QUANTIFICATION AND STATISTICAL ANALYSIS

SUPPLEMENTAL INFORMATION

Supplemental information can be found online at https://doi.org/10.1016/j.isci.2024.109672.

AUTHOR CONTRIBUTIONS

Conceptualization, J.F.N.; investigation, H.T., D.D., and J.F.N.; methodology, H.T., D.D., M.K., K.L., T.S., J.G.L., X.W., and S.B.; formal analysis, H.T., D.D., M.K., K.L., T.S., X.W., and S.B.; validation, H.T., and J.N.J.; writing – original draft, H.T.; writing – review and editing, J.F.N.; funding acquisition, J.F.N.; resources, J.F.N.; project administration, H.T.; supervision, J.F.N. All authors reviewed and approved the final article.

DECLARATION OF INTERESTS

The authors declare no competing interests.

REFERENCES

1. Rassi, A., Jr., Rassi, A., and Marin-Neto, J.A. (2010). Chagas disease. Lancet 375, 1388–1402. https://doi.org/10.1016/S0140-6736(10)60061-X.

2. Lidani, K.C.F., Andrade, F.A., Bavia, L., Damasceno, F.S., Beltrame, M.H., Messias-Reason, I.J., and Sandri, T.L. (2019). Chagas Disease: From Discovery to a Worldwide Health Problem. Front. Public Health 7, 166. https://doi.org/10.3389/fpubh.2019.00166.

3. Cunha-Neto, E., and Chevillard, C. (2014). Chagas disease cardiomyopathy: immunopathology and genetics. Mediat. Inflamm. 2014, 683230. https://doi.org/10.1155/2014/683230.

4. Chadalawada, S., Sillau, S., Archuleta, S., Mundo, W., Bandali, M., Parra-Henao, G., Rodriguez-Morales, A.J., Villamil-Gomez, W.E., Suárez, J.A., Shapiro, L., et al. (2020). Risk of Chronic Cardiomyopathy Among Patients With the Acute Phase or Indeterminate Form of Chagas Disease: A Systematic Review and Meta-analysis. JAMA Netw. Open 3, e2015072. https://doi.org/10.1001/jamanetworkopen.2020.15072.

5. Nunes, M.C.P., Beaton, A., Acquatella, H., Bern, C., Bolger, A.F., Echeverría, L.E., Dutra, W.O., Gascon, J., Morillo, C.A., Oliveira-Filho, J., et al. (2018). Chagas Cardiomyopathy: An Update of Current Clinical Knowledge and Management: A Scientific Statement From the American Heart Association. Circulation 138, e169–e209. https://doi.org/10.1161/CIR.0000000000000599.

6. Camargo, E.P., Gazzinelli, R.T., Morel, C.M., and Precioso, A.R. (2022). Why do we still have not a vaccine against Chagas disease? Mem. Inst. Oswaldo Cruz 117, e200314. https://doi.org/10.1590/0074-02760200314.

7. Rocha, I.H., Ferreira Marques, A.L., Moraes, G.V., Alves da Silva, D.A., Silva, M.V.D., Rodrigues, V., Cunha, D.F.D., and Correia, D. (2020). Metabolic and immunological evaluation of patients with indeterminate and cardiac forms of Chagas disease. Medicine (Baltim.) 99, e23773. https://doi.org/10.1097/MD.0000000000023773.

8. Lizardo, K., Ayyappan, J.P., Cui, M.H., Balasubramanya, R., Jelicks, L.A., and Nagajyothi, J.F. (2019). High fat diet aggravates cardiomyopathy in murine chronic Chagas disease. Microb. Infect. 21,

63–71. https://doi.org/10.1016/j.micinf.2018.07.001.

9. Ayyappan, J.P., Lizardo, K., Wang, S., Yurkow, E., and Nagajyothi, J.F. (2019). Inhibition of ER Stress by 2-Aminopurine Treatment Modulates Cardiomyopathy in a Murine Chronic Chagas Disease Model. Biomol. Ther. 27, 386–394. https://doi.org/10.4062/biomolther.2018.193.

10. Ayyappan, J.P., Lizardo, K., Wang, S., Yurkow, E., and Nagajyothi, J.F. (2020). Inhibition of SREBP Improves Cardiac Lipidopathy, Improves Endoplasmic Reticulum Stress, and Modulates Chronic Chagas Cardiomyopathy. J. Am. Heart Assoc. 9, e014255. https://doi.org/10.1161/JAHA.119.014255.

11. Lizardo, K., Ayyappan, J.P., Oswal, N., Weiss, L.M., Scherer, P.E., and Nagajyothi, J.F. (2021). Fat tissue regulates the pathogenesis and severity of cardiomyopathy in murine chagas disease. PLoS Neglected Trop. Dis. 15, e0008964. https://doi.org/10.1371/journal.pntd.0008964.

12. Marelli-Berg, F.M., and Aksentijevic, D. (2019). Immunometabolic cross-talk in the inflamed heart. Cell Stress 3, 240–266. https://doi.org/10.15698/cst2019.08.194.

13. Choe, S.S., Huh, J.Y., Hwang, I.J., Kim, J.I., and Kim, J.B. (2016). Adipose Tissue Remodeling: Its Role in Energy Metabolism and Metabolic Disorders. Front. Endocrinol. 7, 30. https://doi.org/10.3389/fendo.2016.00030.

14. Luo, L., and Liu, M. (2016). Adipose tissue in control of metabolism. J. Endocrinol. 231, R77–R99. https://doi.org/10.1530/JOE-16-0211.

15. Dragoo, J.L., Shapiro, S.A., Bradsell, H., and Frank, R.M. (2021). The essential roles of human adipose tissue: Metabolic, thermoregulatory, cellular, and paracrine effects. J. Cartil. Jt. Preserv. 1, 100023.

16. Samanta, R., Pouliopoulos, J., Thiagalingam, A., and Kovoor, P. (2016). Role of adipose tissue in the pathogenesis of cardiac arrhythmias. Heart Rhythm 13, 311–320. https://doi.org/10.1016/j.hrthm.2015.08.016.

17. Combs, T.P., Nagajyothi, Mukherjee, S., de Almeida, C.J.G., Jelicks, L.A., Schubert, W., Lin, Y., Jayabalan, D.S., Zhao, D., Braunstein, V.L., et al. (2005). The adipocyte as an important target cell for Trypanosoma cruzi infection. J. Biol. Chem. 280, 24085–24094. https://doi.org/10.1074/jbc.M412802200.

18. Nagajyothi, F., Machado, F.S., Burleigh, B.A., Jelicks, L.A., Scherer, P.E., Mukherjee, S., Lisanti, M.P., Weiss, L.M., Garg, N.J., and Tanowitz, H.B. (2012). Mechanisms of Trypanosoma cruzi persistence in Chagas disease. Cell Microbiol. 14, 634–643. https://doi.org/10.1111/j.1462-5822.2012.01764.x.

19. Biagiotti, M., Dominguez, S., Yamout, N., and Zufferey, R. (2017). Lipidomics and anti-trypanosomatid chemotherapy. Clin. Transl. Med. 6, 27. https://doi.org/10.1186/s40169-017-0160-7.

20. Zuzarte-Luís, V., and Mota, M.M. (2018). Parasite Sensing of Host Nutrients and Environmental Cues. Cell Host Microbe 23, 749–758. https://doi.org/10.1016/j.chom.2018.05.018.

21. Blandin, A., Amosse, J., Froger, J., Hilairet, G., Durcin, M., Fizanne, L., Ghesquière, V., Prieur, X., Chaigneau, J., Vergori, L., et al. (2023). Extracellular vesicles are carriers of adiponectin with insulin-sensitizing and anti-inflammatory properties. Cell Rep. 42, 112866. https://doi.org/10.1016/j.celrep.2023.112866.

22. Blandin, A., Dugail, I., Hilairet, G., Ponnaiah, M., Ghesquière, V., Froger, J., Ducheix, S., Fizanne, L., Boursier, J., Cariou, B., et al. (2023). Lipidomic analysis of adipose-derived extracellular vesicles reveals specific EV lipid sorting informative of the obesity metabolic state. Cell Rep. 42, 112169. https://doi.org/10.1016/j.celrep.2023.112169.

23. Prins, J.B., Niesler, C.U., Winterford, C.M., Bright, N.A., Siddle, K., O'Rahilly, S., Walker, N.I., and Cameron, D.P. (1997). Tumor necrosis factor-alpha induces apoptosis of human adipose cells. Diabetes 46, 1939–1944. https://doi.org/10.2337/diab.46.12.1939.

24. Wen, J.J., Nagajyothi, F., Machado, F.S., Weiss, L.M., Scherer, P.E., Tanowitz, H.B., and Garg, N.J. (2014). Markers of oxidative stress in adipose tissue during Trypanosoma cruzi infection. Parasitol. Res. 113, 3159–3165. https://doi.org/10.1007/s00436-014-3977-7.

25. Nagajyothi, J.F., and Weiss, L.M. (2019). Advances in understanding the role of adipose tissue and mitochondrial oxidative stress in Trypanosoma cruzi infection. F1000Res. 8. F1000 Faculty Rev-1152. https://doi.org/10.12688/f1000research.19190.1.

26. Nagajyothi, F., Desruisseaux, M.S., Machado, F.S., Upadhya, R., Zhao, D., Schwartz, G.J., Teixeira, M.M., Albanese, C., Lisanti, M.P., Chua, S.C., Jr., et al. (2012). Response of adipose tissue to early infection with Trypanosoma cruzi (Brazil strain). J. Infect. Dis. 205, 830–840. https://doi.org/10.1093/infdis/jir840.

27. Fitzgibbons, T.P., and Czech, M.P. (2014). Epicardial and perivascular adipose tissues and their influence on cardiovascular disease: basic mechanisms and clinical associations. J. Am. Heart Assoc. 3, e000582. https://doi.org/10.1161/JAHA.113.000582.

28. Bale, L.K., West, S.A., and Conover, C.A. (2018). Characterization of mouse pericardial fat: regulation by PAPP-A. Growth Hormone IGF Res. 42–43, 1–7. https://doi.org/10.1016/j.ghir.2018.07.002.

29. Raposo, G., and Stoorvogel, W. (2013). Extracellular vesicles: exosomes, microvesicles, and friends. J. Cell Biol. 200, 373–383. https://doi.org/10.1083/jcb.201211138.

30. Borges, F.T., Reis, L.A., and Schor, N. (2013). Extracellular vesicles: structure, function, and potential clinical uses in renal diseases. Braz. J. Med. Biol. Res. 46, 824–830. https://doi.org/10.1590/1414-431X20132964.

31. Mashouri, L., Yousefi, H., Aref, A.R., Ahadi, A.M., Molaei, F., and Alahari, S.K. (2019). Exosomes: composition, biogenesis, and mechanisms in cancer metastasis and drug resistance. Mol. Cancer 18, 75. https://doi.org/10.1186/s12943-019-0991-5.

32. Yáñez-Mó, M., Siljander, P.R.M., Andreu, Z., Zavec, A.B., Borràs, F.E., Buzas, E.I., Buzas, K., Casal, E., Cappello, F., Carvalho, J., et al. (2015). Biological properties of extracellular vesicles and their physiological functions. J. Extracell. Vesicles 4, 27066. https://doi.org/10.3402/jev.v4.27066.

33. Kakarla, R., Hur, J., Kim, Y.J., Kim, J., and Chwae, Y.J. (2020). Apoptotic cell-derived exosomes: messages from dying cells. Exp. Mol. Med. 52, 1–6. https://doi.org/10.1038/s12276-019-0362-8.

34. Stewart, S., Gessler, F., Pluchino, S., and Moreau, K. (2016). Inside-out: Unpredicted Annexin A2 Localisation on the Surface of Extracellular Vesicles (ScienceMatters). https://doi.org/10.19185/matters.201602000015.

35. Stewart, S.E., Ashkenazi, A., Williamson, A., Rubinsztein, D.C., and Moreau, K. (2018). Phospholipid flipping facilitates annexin translocation across membranes. Preprint at bioRxiv. https://doi.org/10.1101/241976.

36. Shah, N., Ishii, M., Brandon, C., Ablonczy, Z., Cai, J., Liu, Y., Chou, C.J., and Rohrer, B. (2018). Extracellular vesicle-mediated long-range communication in stressed retinal pigment epithelial cell monolayers. Biochim. Biophys. Acta, Mol. Basis Dis. 1864, 2610–2622. https://doi.org/10.1016/j.bbadis.2018.04.016.

37. Botha, J., Handberg, A., and Simonsen, J.B. (2022). Lipid-based strategies used to identify extracellular vesicles in flow cytometry can be confounded by lipoproteins: Evaluations of annexin V, lactadherin, and detergent lysis. J. Extracell. Vesicles 11, e12200. https://doi.org/10.1002/jev2.12200.

38. Lee, J.E., Moon, P.G., Lee, I.K., and Baek, M.C. (2015). Proteomic Analysis of Extracellular Vesicles Released by Adipocytes of Otsuka Long-Evans Tokushima Fatty (OLETF) Rats. Protein J. 34, 220–235. https://doi.org/10.1007/s10930-015-9616-z.

39. Stroh, A.M., Lynch, C.E., Lester, B.E., Minchev, K., Chambers, T.L., Montenegro, C.F., Chavez Martinez, C., Fountain, W.A., Trappe, T.A., and Trappe, S.W. (2021). Human adipose and skeletal muscle tissue DNA, RNA, and protein content. J. Appl. Physiol. 131, 1370–1379. https://doi.org/10.1152/japplphysiol.00343.2021.

40. Chen, H., Wang, Z., Qin, M., Zhang, B., Lin, L., Ma, Q., Liu, C., Chen, X., Li, H., Lai, W., and Zhong, S. (2021). Comprehensive Metabolomics Identified the Prominent Role of Glycerophospholipid Metabolism in Coronary Artery Disease Progression. Front. Mol. Biosci. 8, 632950. https://doi.org/10.3389/fmolb.2021.632950.

41. Borodzicz-Jażdżyk, S., Jażdżyk, P., Łysik, W., Cudnoch-Jędrzejewska, A., and Czarzasta, K. (2022). Sphingolipid metabolism and signaling in cardiovascular diseases. Front. Cardiovasc. Med. 9, 915961. https://doi.org/10.3389/fcvm.2022.915961.

42. Sun, H., Sun, S., Chen, G., Xie, H., Yu, S., Lin, X., Qian, J., Mao, C., Peng, H., Chen, H., et al. (2021). Ceramides and sphingosine-1-phosphate mediate the distinct effects of M1/M2-macrophage infusion on liver recovery after hepatectomy. Cell Death Dis. 12, 324. https://doi.org/10.1038/s41419-021-03616-9.

43. Aflaki, E., Radovic, B., Chandak, P.G., Kolb, D., Eisenberg, T., Ring, J., Fertschai, I., Uellen, A., Wolinski, H., Kohlwein, S.D., et al. (2011). Triacylglycerol accumulation activates the mitochondrial apoptosis pathway in macrophages. J. Biol. Chem. 286, 7418–7428. https://doi.org/10.1074/jbc.M110.175703.

44. Von Bank, H., Hurtado-Thiele, M., Oshimura, N., and Simcox, J. (2021). Mitochondrial Lipid Signaling and Adaptive Thermogenesis. Metabolites 11, 124. https://doi.org/10.3390/metabo11020124.

45. Lizaso, A., Tan, K.T., and Lee, Y.H. (2013). beta-adrenergic receptor-stimulated lipolysis requires the RAB7-mediated autolysosomal lipid degradation. Autophagy *9*, 1228–1243. https://doi.org/10.4161/auto.24893.

46. Blaser, H., Dostert, C., Mak, T.W., and Brenner, D. (2016). TNF and ROS Crosstalk in Inflammation. Trends Cell Biol. *26*, 249–261. https://doi.org/10.1016/j.tcb.2015.12.002.

47. Dalal, S., Foster, C.R., Das, B.C., Singh, M., and Singh, K. (2012). Beta-adrenergic receptor stimulation induces endoplasmic reticulum stress in adult cardiac myocytes: role in apoptosis. Mol. Cell. Biochem. *364*, 59–70. https://doi.org/10.1007/s11010-011-1205-7.

48. Deng, J., Jiang, Y., Chen, Z.B., Rhee, J.W., Deng, Y., and Wang, Z.V. (2023). Mitochondrial Dysfunction in Cardiac Arrhythmias. Cells *12*, 679. https://doi.org/10.3390/cells12050679.

49. Yang, K.C., Bonini, M.G., and Dudley, S.C., Jr. (2014). Mitochondria and arrhythmias. Free Radic. Biol. Med. *71*, 351–361. https://doi.org/10.1016/j.freeradbiomed.2014.03.033.

50. Saadeh, K., and Fazmin, I.T. (2021). Mitochondrial Dysfunction Increases Arrhythmic Triggers and Substrates; Potential Anti-arrhythmic Pharmacological Targets. Front. Cardiovasc. Med. *8*, 646932. https://doi.org/10.3389/fcvm.2021.646932.

51. Vinhas, M., Araújo, A.C., Ribeiro, S., Rosário, L.B., and Belo, J.A. (2013). Transthoracic echocardiography reference values in juvenile and adult 129/Sv mice. Cardiovasc. Ultrasound *11*, 12. https://doi.org/10.1186/1476-7120-11-12.

52. Sørensen, L.L., Bedja, D., Sysa-Shah, P., Liu, H., Maxwell, A., Yi, X., Pozios, I., Olsen, N.T., Abraham, T.P., Abraham, R., and Gabrielson, K. (2016). Echocardiographic Characterization of a Murine Model of Hypertrophic Obstructive Cardiomyopathy Induced by Cardiac-specific Overexpression of Epidermal Growth Factor Receptor 2. Comp. Med. *66*, 268–277.

53. AHA (2023). Ejection Fraction Heart Failure Measurement. https://www.heart.org/en/health-topics/heart-failure/diagnosing-heart-failure/ejection-fraction-heart-failure-measurement.

54. Xu, Y., Zhang, Y., and Ye, J. (2018). IL-6: A Potential Role in Cardiac Metabolic Homeostasis. Int. J. Mol. Sci. *19*, 2474. https://doi.org/10.3390/ijms19092474.

55. van Hall, G., Steensberg, A., Sacchetti, M., Fischer, C., Keller, C., Schjerling, P., Hiscock, N., Møller, K., Saltin, B., Febbraio, M.A., and Pedersen, B.K. (2003). Interleukin-6 stimulates lipolysis and fat oxidation in humans. J. Clin. Endocrinol. Metab. *88*, 3005–3010. https://doi.org/10.1210/jc.2002-021687.

56. Marcinkiewicz, A., Gauthier, D., Garcia, A., and Brasaemle, D.L. (2006). The phosphorylation of serine 492 of perilipin a directs lipid droplet fragmentation and dispersion. J. Biol. Chem. *281*, 11901–11909. https://doi.org/10.1074/jbc.M600171200.

57. Bougarne, N., Weyers, B., Desmet, S.J., Deckers, J., Ray, D.W., Staels, B., and De Bosscher, K. (2018). Molecular Actions of PPARalpha in Lipid Metabolism and Inflammation. Endocr. Rev. *39*, 760–802. https://doi.org/10.1210/er.2018-00064.

58. Guerra, I.M.S., Ferreira, H.B., Melo, T., Rocha, H., Moreira, S., Diogo, L., Domingues, M.R., and Moreira, A.S.P. (2022). Mitochondrial Fatty Acid beta-Oxidation Disorders: From Disease to Lipidomic Studies-A Critical Review. Int. J. Mol. Sci. *23*, 13933. https://doi.org/10.3390/ijms232213933.

59. Cnop, M., Toivonen, S., Igoillo-Esteve, M., and Salpea, P. (2017). Endoplasmic reticulum stress and eIF2alpha phosphorylation: The Achilles heel of pancreatic beta cells. Mol. Metabol. *6*, 1024–1039. https://doi.org/10.1016/j.molmet.2017.06.001.

60. Szegezdi, E., Logue, S.E., Gorman, A.M., and Samali, A. (2006). Mediators of endoplasmic reticulum stress-induced apoptosis. EMBO Rep. *7*, 880–885. https://doi.org/10.1038/sj.embor.7400779.

61. Oslowski, C.M., and Urano, F. (2011). Measuring ER stress and the unfolded protein response using mammalian tissue culture system. Methods Enzymol. *490*, 71–92. https://doi.org/10.1016/B978-0-12-385114-7.00004-0.

62. Chandra, D., Choy, G., and Tang, D.G. (2007). Cytosolic accumulation of HSP60 during apoptosis with or without apparent mitochondrial release: evidence that its pro-apoptotic or pro-survival functions involve differential interactions with caspase-3. J. Biol. Chem. *282*, 31289–31301. https://doi.org/10.1074/jbc.M702777200.

63. Martinus, R.D., and Goldsbury, J. (2018). Endothelial TNF-alpha induction by Hsp60 secreted from THP-1 monocytes exposed to hyperglycaemic conditions. Cell Stress Chaperones *23*, 519–525. https://doi.org/10.1007/s12192-017-0858-x.

64. Labovsky, V., Smulski, C.R., Gómez, K., Levy, G., and Levin, M.J. (2007). Anti-beta1-adrenergic receptor autoantibodies in patients with chronic Chagas heart disease. Clin. Exp. Immunol. *148*, 440–449. https://doi.org/10.1111/j.1365-2249.2007.03381.x.

65. Higuchi, M.d.L., Benvenuti, L.A., Martins Reis, M., and Metzger, M. (2003). Pathophysiology of the heart in Chagas' disease: current status and new developments. Cardiovasc. Res. *60*, 96–107. https://doi.org/10.1016/s0008-6363(03)00361-4.

66. Yoo, B., Lemaire, A., Mangmool, S., Wolf, M.J., Curcio, A., Mao, L., and Rockman, H.A. (2009). Beta1-adrenergic receptors stimulate cardiac contractility and CaMKII activation *in vivo* and enhance cardiac dysfunction following myocardial infarction. Am. J. Physiol. Heart Circ. Physiol. *297*, H1377–H1386. https://doi.org/10.1152/ajpheart.00504.2009.

67. Zhang, Y., Hou, M.C., Li, J.J., Qi, Y., Zhang, Y., She, G., Ren, Y.J., Wu, W., Pang, Z.D., Xie, W., et al. (2020). Cardiac beta-adrenergic receptor activation mediates distinct and cell type-dependent changes in the expression and distribution of connexin 43. J. Cell Mol. Med. *24*, 8505–8517. https://doi.org/10.1111/jcmm.15469.

68. Nagajyothi, F., Weiss, L.M., Zhao, D., Koba, W., Jelicks, L.A., Cui, M.H., Factor, S.M., Scherer, P.E., and Tanowitz, H.B. (2014). High fat diet modulates Trypanosoma cruzi infection associated myocarditis. PLoS Neglected Trop. Dis. *8*, e3118. https://doi.org/10.1371/journal.pntd.0003118.

69. Trindade, S., Rijo-Ferreira, F., Carvalho, T., Pinto-Neves, D., Guegan, F., Aresta-Branco, F., Bento, F., Young, S.A., Pinto, A., Van Den Abbeele, J., et al. (2016). Trypanosoma brucei Parasites Occupy and Functionally Adapt to the Adipose Tissue in Mice. Cell Host Microbe *19*, 837–848. https://doi.org/10.1016/j.chom.2016.05.002.

70. Ayyappan, J.P., and Nagajyothi, J.F. (2017). Diet Modulates Adipose Tissue Oxidative Stress in a Murine Acute Chagas Model. JSM Atheroscler. *2*, 1030.

71. Lizardo, K., Almonte, V., Law, C., Aiyyappan, J.P., Cui, M.H., and Nagajyothi, J.F. (2017). Diet regulates liver autophagy differentially in murine acute Trypanosoma cruzi infection. Parasitol. Res. *116*, 711–723. https://doi.org/10.1007/s00436-016-5337-2.

72. Beigier-Bompadre, M., Montagna, G.N., Kühl, A.A., Lozza, L., Weiner, J., 3rd, Kupz, A., Vogelzang, A., Mollenkopf, H.J., Löwe, D., Bandermann, S., et al. (2017). Mycobacterium tuberculosis infection modulates adipose tissue biology. PLoS Pathog. *13*, e1006676. https://doi.org/10.1371/journal.ppat.1006676.

73. Ayyappan, J.P., Vinnard, C., Subbian, S., and Nagajyothi, J.F. (2018). Effect of Mycobacterium tuberculosis infection on adipocyte physiology. Microb. Infect. *20*, 81–88. https://doi.org/10.1016/j.micinf.2017.10.008.

74. González, F.B., Villar, S.R., Toneatto, J., Pacini, M.F., Márquez, J., D'Attilio, L., Bottasso, O.A., Piwien-Pilipuk, G., and Pérez, A.R. (2019). Immune response triggered by Trypanosoma cruzi infection strikes adipose tissue homeostasis altering lipid storage, enzyme profile and adipokine expression. Med. Microbiol. Immunol. *208*, 651–666. https://doi.org/10.1007/s00430-018-0572-z.

75. Ayyappan, J.P., Ganapathi, U., Lizardo, K., Vinnard, C., Subbian, S., Perlin, D.S., and Nagajyothi, J.F. (2019). Adipose Tissue Regulates Pulmonary Pathology during TB Infection. mBio *10*, e02771-18. https://doi.org/10.1128/mBio.02771-18.

76. Dhanyalayam, D., Thangavel, H., Lizardo, K., Oswal, N., Dolgov, E., Perlin, D.S., and Nagajyothi, J.F. (2022). Sex Differences in Cardiac Pathology of SARS-CoV2 Infected and Trypanosoma cruzi Co-infected Mice. Front. Cardiovasc. Med. *9*, 783974. https://doi.org/10.3389/fcvm.2022.783974.

77. Martínez-Colón, G.J., Ratnasiri, K., Chen, H., Jiang, S., Zanley, E., Rustagi, A., Verma, R., Chen, H., Andrews, J.R., Mertz, K.D., et al. (2022). SARS-CoV-2 infection drives an inflammatory response in human adipose tissue through infection of adipocytes and macrophages. Sci. Transl. Med. *14*, eabm9151. https://doi.org/10.1126/scitranslmed.abm9151.

78. Thangavel, H., Dhanyalayam, D., Lizardo, K., Oswal, N., Dolgov, E., Perlin, D.S., and Nagajyothi, J.F. (2023). Susceptibility of Fat Tissue to SARS-CoV-2 Infection in Female hACE2 Mouse Model. Int. J. Mol. Sci. *24*, 1314. https://doi.org/10.3390/ijms24021314.

79. Sykes, M.L., Kennedy, E.K., and Avery, V.M. (2023). Impact of Laboratory-Adapted Intracellular Trypanosoma cruzi Strains on the Activity Profiles of Compounds with Anti-T. cruzi Activity. Microorganisms *11*, 476. https://doi.org/10.3390/microorganisms11020476.

80. Jung, T.W., Park, T., Park, J., Kim, U., Je, H.D., Kim, H.D., Cho, S.W., Abd El-Aty, A.M., Song, J.H., Kim, H.C., et al. (2019).

Phosphatidylcholine causes adipocyte-specific lipolysis and apoptosis in adipose and muscle tissues. PLoS One 14, e0214760. https://doi.org/10.1371/journal.pone.0214760.

81. Röszer, T. (2021). Adipose Tissue Immunometabolism and Apoptotic Cell Clearance. Cells 10, 2288. https://doi.org/10.3390/cells10092288.

82. Barros, F.M., Carneiro, F., Machado, J.C., and Melo, S.A. (2018). Exosomes and Immune Response in Cancer: Friends or Foes? Front. Immunol. 9, 730. https://doi.org/10.3389/fimmu.2018.00730.

83. Durcin, M., Fleury, A., Taillebois, E., Hilairet, G., Krupova, Z., Henry, C., Truchet, S., Trötzmüller, M., Köfeler, H., Mabilleau, G., et al. (2017). Characterisation of adipocyte-derived extracellular vesicle subtypes identifies distinct protein and lipid signatures for large and small extracellular vesicles. J. Extracell. Vesicles 6, 1305677. https://doi.org/10.1080/20013078.2017.1305677.

84. Rome, S., Blandin, A., and Le Lay, S. (2021). Adipocyte-Derived Extracellular Vesicles: State of the Art. Int. J. Mol. Sci. 22, 1788. https://doi.org/10.3390/ijms22041788.

85. Kovilakath, A., and Cowart, L.A. (2020). Sphingolipid Mediators of Myocardial Pathology. J. Lipid Atheroscler. 9, 23–49. https://doi.org/10.12997/jla.2020.9.1.23.

86. Park, T.S., Hu, Y., Noh, H.L., Drosatos, K., Okajima, K., Buchanan, J., Tuinei, J., Homma, S., Jiang, X.C., Abel, E.D., and Goldberg, I.J. (2008). Ceramide is a cardiotoxin in lipotoxic cardiomyopathy. J. Lipid Res. 49, 2101–2112. https://doi.org/10.1194/jlr.M800147-JLR200.

87. Bekhite, M., González-Delgado, A., Hübner, S., Haxhikadrija, P., Kretzschmar, T., Müller, T., Wu, J.M.F., Bekfani, T., Franz, M., Wartenberg, M., et al. (2021). The role of ceramide accumulation in human induced pluripotent stem cell-derived cardiomyocytes on mitochondrial oxidative stress and mitophagy. Free Radic. Biol. Med. 167, 66–80. https://doi.org/10.1016/j.freeradbiomed.2021.02.016.

88. Shu, H., Peng, Y., Hang, W., Li, N., Zhou, N., and Wang, D.W. (2022). Emerging Roles of Ceramide in Cardiovascular Diseases. Aging Dis. 13, 232–245. https://doi.org/10.14336/AD.2021.0710.

89. Aflaki, E., Doddapattar, P., Radović, B., Povoden, S., Kolb, D., Vujić, N., Wegscheider, M., Koefeler, H., Hornemann, T., Graier, W.F., et al. (2012). C16 ceramide is crucial for triacylglycerol-induced apoptosis in macrophages. Cell Death Dis. 3, e280. https://doi.org/10.1038/cddis.2012.17.

90. Jennings, M.J., Hathazi, D., Nguyen, C.D.L., Munro, B., Münchberg, U., Ahrends, R., Schenck, A., Eidhof, I., Freier, E., Synofzik, M., et al. (2021). Intracellular Lipid Accumulation and Mitochondrial Dysfunction Accompanies Endoplasmic Reticulum Stress Caused by Loss of the Co-chaperone DNAJC3. Front. Cell Dev. Biol. 9, 710247. https://doi.org/10.3389/fcell.2021.710247.

91. Kim, J.A., Wei, Y., and Sowers, J.R. (2008). Role of mitochondrial dysfunction in insulin resistance. Circ. Res. 102, 401–414. https://doi.org/10.1161/CIRCRESAHA.107.165472.

92. Kratky, D., Obrowsky, S., Kolb, D., and Radovic, B. (2014). Pleiotropic regulation of mitochondrial function by adipose triglyceride lipase-mediated lipolysis.

93. Biochimie 96, 106–112. https://doi.org/10.1016/j.biochi.2013.06.023.

93. Viola, A., Munari, F., Sánchez-Rodríguez, R., Scolaro, T., and Castegna, A. (2019). The Metabolic Signature of Macrophage Responses. Front. Immunol. 10, 1462. https://doi.org/10.3389/fimmu.2019.01462.

94. Ferré, P., Phan, F., and Foufelle, F. (2021). SREBP-1c and lipogenesis in the liver: an update1. Biochem. J. 478, 3723–3739. https://doi.org/10.1042/BCJ20210071.

95. Chen, Y., Pat, B., Zheng, J., Cain, L., Powell, P., Shi, K., Sabri, A., Husain, A., and Dell'italia, L.J. (2010). Tumor necrosis factor-alpha produced in cardiomyocytes mediates a predominant myocardial inflammatory response to stretch in early volume overload. J. Mol. Cell. Cardiol. 49, 70–78. https://doi.org/10.1016/j.yjmcc.2009.12.013.

96. Li, Z., Zhou, J., Zhu, D., Zhang, Q., Huang, M., Han, Y., and Zhou, S. (2015). Role of endogenous TNF-α in cardiomyocyte apoptosis induced by bacteria lipoprotein and the protective effect of IL-10. Eur. J. Inflamm. 13, 117–125. https://doi.org/10.1177/1721727x15597363.

97. Gandoy-Fieiras, N., Gonzalez-Juanatey, J.R., and Eiras, S. (2020). Myocardium Metabolism in Physiological and Pathophysiological States: Implications of Epicardial Adipose Tissue and Potential Therapeutic Targets. Int. J. Mol. Sci. 21, 2641. https://doi.org/10.3390/ijms21072641.

98. Wu, Y., Zhang, A., Hamilton, D.J., and Deng, T. (2017). Epicardial Fat in the Maintenance of Cardiovascular Health. Methodist Debakey Cardiovasc. J. 13, 20–24. https://doi.org/10.14797/mdcj-13-1-20.

99. Hopkins, T.A., Ouchi, N., Shibata, R., and Walsh, K. (2007). Adiponectin actions in the cardiovascular system. Cardiovasc. Res. 74, 11–18. https://doi.org/10.1016/j.cardiores.2006.10.009.

100. Ouchi, N., Shibata, R., and Walsh, K. (2006). Cardioprotection by adiponectin. Trends Cardiovasc. Med. 16, 141–146. https://doi.org/10.1016/j.tcm.2006.03.001.

101. Bennett, M.R. (2002). Apoptosis in the cardiovascular system. Heart 87, 480–487. https://doi.org/10.1136/heart.87.5.480.

102. Ni, L., Zhou, C., Duan, Q., Lv, J., Fu, X., Xia, Y., and Wang, D.W. (2011). beta-AR blockers suppresses ER stress in cardiac hypertrophy and heart failure. PLoS One 6, e27294. https://doi.org/10.1371/journal.pone.0027294.

103. Hosoi, T., Honda, M., Oba, T., and Ozawa, K. (2013). ER stress upregulated PGE(2)/IFNgamma-induced IL-6 expression and down-regulated iNOS expression in glial cells. Sci. Rep. 3, 3388. https://doi.org/10.1038/srep03388.

104. Sanchez, C.L., Sims, S.G., Nowery, J.D., and Meares, G.P. (2019). Endoplasmic reticulum stress differentially modulates the IL-6 family of cytokines in murine astrocytes and macrophages. Sci. Rep. 9, 14931. https://doi.org/10.1038/s41598-019-51481-6.

105. Nash, C.A., Wei, W., Irannejad, R., and Smrcka, A.V. (2019). Golgi localized beta1-adrenergic receptors stimulate Golgi PI4P hydrolysis by PLCepsilon to regulate cardiac hypertrophy. Elife 8, e48167. https://doi.org/10.7554/eLife.48167.

106. Zimmer, H.G., Kolbeck-Ruhmkorff, C., and Zierhut, W. (1995). Cardiac hypertrophy induced by alpha- and beta-adrenergic

receptor stimulation. Cardioscience 6, 47–57.

107. Osadchii, O.E. (2007). Cardiac hypertrophy induced by sustained beta-adrenoreceptor activation: pathophysiological aspects. Heart Fail. Rev. 12, 66–86. https://doi.org/10.1007/s10741-007-9007-4.

108. Cardoso, C.S., Sabino, E.C., Oliveira, C.D.L., de Oliveira, L.C., Ferreira, A.M., Cunha-Neto, E., Bierrenbach, A.L., Ferreira, J.E., Haikal, D.S., Reingold, A.L., and Ribeiro, A.L.P. (2016). Longitudinal study of patients with chronic Chagas cardiomyopathy in Brazil (SaMi-Trop project): a cohort profile. BMJ Open 6, e011181. https://doi.org/10.1136/bmjopen-2016-011181.

109. Pastore, C.A., Samesima, N., Pereira Filho, H.G., Varoni, L.P.C., Rochitte, C.E., Vieira, M.L., Ávila, L.F.R.d., Melo, R.d.J.L., Pereira, A.d.C., Daheer, J., and Carlo, C.H.d. (2015). Rare Association: Chagas' Disease and Hypertrophic Cardiomyopathy. Ann. Noninvasive Electrocardiol. 20, 498–501. https://doi.org/10.1111/anec.12229.

110. Liu, Y., Wang, M., Yu, Y., Li, C., and Zhang, C. (2023). Advances in the study of exosomes derived from mesenchymal stem cells and cardiac cells for the treatment of myocardial infarction. Cell Commun. Signal. 21, 202. https://doi.org/10.1186/s12964-023-01227-9.

111. Liang, B., He, X., Zhao, Y.X., Zhang, X.X., and Gu, N. (2020). Advances in Exosomes Derived from Different Cell Sources and Cardiovascular Diseases. BioMed Res. Int. 2020, 7298687. https://doi.org/10.1155/2020/7298687.

112. Cortes-Serra, N., Gualdron-Lopez, M., Pinazo, M.J., Torrecilhas, A.C., and Fernandez-Becerra, C. (2022). Extracellular Vesicles in Trypanosoma cruzi Infection: Immunomodulatory Effects and Future Perspectives as Potential Control Tools against Chagas Disease. J. Immunol. Res. 2022, 5230603. https://doi.org/10.1155/2022/5230603.

113. D'Avila, H., de Souza, N.P., Albertoni, A.L.D.S., Campos, L.C., Rampinelli, P.G., Correa, J.R., and de Almeida, P.E. (2021). Impact of the Extracellular Vesicles Derived From Trypanosoma cruzi: A Paradox in Host Response and Lipid Metabolism Modulation. Front. Cell. Infect. Microbiol. 11, 768124. https://doi.org/10.3389/fcimb.2021.768124.

114. Kulaj, K., Harger, A., Bauer, M., Caliskan, Ö.S., Gupta, T.K., Chiang, D.M., Milbank, E., Reber, J., Karlas, A., Kotzbeck, P., et al. (2023). Adipocyte-derived extracellular vesicles increase insulin secretion through transport of insulinotropic protein cargo. Nat. Commun. 14, 709. https://doi.org/10.1038/s41467-023-36148-1.

115. Gesmundo, I., Pardini, B., Gargantini, E., Gamba, G., Birolo, G., Fanciulli, A., Banfi, D., Congiusta, N., Favaro, E., Deregibus, M.C., et al. (2021). Adipocyte-derived extracellular vesicles regulate survival and function of pancreatic beta cells. JCI Insight 6, e141962. https://doi.org/10.1172/jci.insight.141962.

116. Schneider, C.A., Rasband, W.S., and Eliceiri, K.W. (2012). NIH Image to ImageJ: 25 years of image analysis. Nat. Methods 9, 671–675. https://doi.org/10.1038/nmeth.2089.

117. Pang, Z., Chong, J., Zhou, G., de Lima Morais, D.A., Chang, L., Barrette, M., Gauthier, C., Jacques, P.É., Li, S., and Xia, J. (2021). MetaboAnalyst 5.0: narrowing the gap between raw spectra and functional

insights. Nucleic Acids Res. *49*, W388–W396. https://doi.org/10.1093/nar/gkab382.

118. Mott, A., Lenormand, G., Costales, J., Fredberg, J.J., and Burleigh, B.A. (2009). Modulation of host cell mechanics by Trypanosoma cruzi. J. Cell. Physiol. *218*, 315–322. https://doi.org/10.1002/jcp.21606.

119. Zhao, D., Lizardo, K., Cui, M.H., Ambadipudi, K., Lora, J., Jelicks, L.A., and Nagajyothi, J.F. (2016). Antagonistic effect of atorvastatin on high fat diet induced survival during acute Chagas disease. Microb. Infect. *18*, 675–686. https://doi.org/10.1016/j.micinf.2016.06.006.

120. Thangavel, H., Lizardo, K., Dhanyalayam, D., De Assis, S., and Nagajyothi, J.F. (2023). Diets Differently Regulate Tumorigenesis in Young E0771 Syngeneic Breast Cancer Mouse Model. J. Clin. Med. *12*, 413. https://doi.org/10.3390/jcm12020413.

121. Gupta, S., and Knowlton, A.A. (2007). HSP60 trafficking in adult cardiac myocytes: role of the exosomal pathway. Am. J. Physiol. Heart Circ. Physiol. *292*, H3052–H3056. https://doi.org/10.1152/ajpheart.01355.2006.

122. Malonis, R.J., Georgiev, G.I., Haslwanter, D., VanBlargan, L.A., Fallon, G., Vergnolle, O., Cahill, S.M., Harris, R., Cowburn, D., Chandran, K., et al. (2022). A Powassan virus domain III nanoparticle immunogen elicits neutralizing and protective antibodies in mice. PLoS Pathog. *18*, e1010573. https://doi.org/10.1371/journal.ppat.1010573.

123. Mitchell, M.I., Ben-Dov, I.Z., Liu, C., Ye, K., Chow, K., Kramer, Y., Gangadharan, A., Park, S., Fitzgerald, S., Ramnauth, A., et al. (2021). Extracellular Vesicle Capture by AnTibody of CHoice and Enzymatic Release (EV-CATCHER): A customizable purification assay designed for small-RNA biomarker identification and evaluation of circulating small-EVs. J. Extracell. Vesicles *10*, e12110. https://doi.org/10.1002/jev2.12110.

124. Toivonen, R., Koskenvuo, J., Merentie, M., Söderström, M., Ylä-Herttuala, S., and Savontaus, M. (2012). Intracardiac injection of a capsid-modified Ad5/35 results in decreased heart toxicity when compared to standard Ad5. Virol. J. *9*, 296. https://doi.org/10.1186/1743-422X-9-296.

STAR★METHODS

KEY RESOURCES TABLE

REAGENT or RESOURCE	SOURCE	IDENTIFIER
Antibodies		
Goat Polyclonal Anti-Mouse Adiponectin, Biotin Conjugated	R&D Systems	Cat#BAF1119; RRID: AB_2273527
Mouse Monoclonal Anti-Adiponectin	Abcam	Cat#ab22554; RRID: AB_447152
Rabbit Polyclonal Anti-Adiponectin	BioVision	Cat#5901-250; RRID: AB_442498
Rabbit Monoclonal Anti-Fabp4, Biotin Conjugated	Signalway Antibody	Cat#C49511-Biotin; RRID: AB_3095322
Goat Polyclonal Anti-Mouse Fabp4	R&D Systems	Cat#AF1443; RRID: AB_2102444
Rat Monoclonal Anti-Fabp4	R&D Systems	Cat#MAB3150; RRID: AB_3095323
Rabbit Monoclonal Anti-Annexin V	Abcam	Cat#ab108194; RRID: AB_10863755
Rabbit Polyclonal Anti-Annexin V	Cell Signaling Technology	Cat#8555; RRID: AB_10950499
Rabbit Monoclonal Anti-Caspase-7	Cell Signaling Technology	Cat#12827; RRID: AB_2687912
Rabbit Monoclonal Anti-Cleaved Caspase-7	Cell Signaling Technology	Cat#8438; RRID: AB_11178377
Mouse Monoclonal Anti-Phospho-Perilipin 1	Vala Science	Cat#4856; RRID: AB_2909466
Rabbit Polyclonal Anti-Perilipin 1	Thermo Fisher Scientific	Cat#PA5-72921; RRID: AB_2718775
Rabbit Polyclonal Anti-β1-Adrenergic Receptor	Cell Signaling Technology	Cat#12271; RRID: AB_2797865
Mouse Monoclonal Anti-CHOP	Cell Signaling Technology	Cat#2895; RRID: AB_2089254
Rabbit Polyclonal Anti-TNF-α	Cell Signaling Technology	Cat#3707; RRID: AB_2240625
Rabbit Polyclonal Anti-IFNγ	Bioss	Cat#bs-0480R; RRID: AB_10857066
Mouse Monoclonal Anti-IL6	Proteintech	Cat#66146-1-Ig; RRID: AB_2881543
Rat Monoclonal Anti-F4/80	Novus Biologicals	Cat#NB600-404; RRID: AB_10003219
Rabbit Polyclonal Anti-SREBP1	Abcam	Cat#ab28481; RRID: AB_778069
Mouse Monoclonal Anti-PPARα	Thermo Fisher Scientific	Cat#MA1-822; RRID: AB_2165745
Rabbit Monoclonal Anti-SDHA	Cell Signaling Technology	Cat#11998; RRID: AB_2750900
Rabbit Monoclonal Anti-Cytochrome c	Cell Signaling Technology	Cat#4280; RRID: AB_10695410
Rabbit Monoclonal Anti-COX IV	Cell Signaling Technology	Cat#4850; RRID: AB_2085424
Rabbit Monoclonal Anti-HSP60	Cell Signaling Technology	Cat#12165; RRID: AB_2636980
Rabbit Monoclonal Anti-BiP	Cell Signaling Technology	Cat#3177; RRID: AB_2119845
Rabbit Monoclonal Anti-Phospho-eIF2α	Cell Signaling Technology	Cat#3398; RRID: AB_2096481
Rabbit Monoclonal Anti-PDI	Cell Signaling Technology	Cat#3501; RRID: AB_2156433
Rabbit Polyclonal Anti-BNIP3	Cell Signaling Technology	Cat#3769; RRID: AB_2259284
Rabbit Polyclonal Anti-ANP	Thermo Fisher Scientific	Cat#711569; RRID: AB_2662341
Rabbit Polyclonal Anti-β-actin	Cell Signaling Technology	Cat#4967; RRID: AB_330288
Rabbit Polyclonal Anti-GDI1	Thermo Fisher Scientific	Cat#71-0300; RRID: AB_2533970
Horse Anti-mouse IgG, HRP-conjugated	Cell Signaling Technology	Cat#7076; RRID: AB_330924
Goat Anti-rabbit IgG, HRP-conjugated	Cell Signaling Technology	Cat#7074; RRID: AB_2099233
Goat Polyclonal Anti-Rat IgG, HRP-conjugated	Jackson ImmunoResearch Labs	Cat#112-035-003; RRID: AB_2338128
Goat Polyclonal Anti-Mouse IgG, Alexa Fluor™ 488	Thermo Fisher Scientific	Cat#A-11001; RRID: AB_2534069
Goat Polyclonal Anti-Rabbit IgG, Alexa Fluor™ 594	Thermo Fisher Scientific	Cat#A-11012; RRID: AB_2534079

Continued

REAGENT or RESOURCE	SOURCE	IDENTIFIER
Donkey Polyclonal Anti-Goat IgG, Alexa Fluor™ 594	Thermo Fisher Scientific	Cat#A-11058; RRID: AB_2534105
Goat Polyclonal Anti-Rabbit IgG, Alexa Fluor™ 488	Thermo Fisher Scientific	Cat#A-11008; RRID: AB_143165
Goat Polyclonal Anti-Rat IgG, Alexa Fluor™ 488	Thermo Fisher Scientific	Cat#A-11006; RRID: AB_2534074
Biological samples		
Healthy mice and *T. cruzi* infected mice heart tissue	This paper	N/A
Healthy mice and *T. cruzi* infected mice WAT tissue	This paper	N/A
Healthy mice and *T. cruzi* infected mice plasma	This paper	N/A
Chemicals, peptides, and recombinant proteins		
3T3-L1 Differentiation Medium	ZenBio	Cat#DM-2-L1
3T3-L1 Adipocyte Medium	ZenBio	Cat#AM-1-L1
Subcutaneous Preadipocyte Differentiation Medium	ZenBio	Cat#DM-2
Subcutaneous Adipocyte Maintenance Medium	ZenBio	Cat#AM-1
DMEM	Corning	Cat#10-013-CV
Fetal Bovine Serum, heat inactivated	Thermo Fisher Scientific	Cat#16140071
Penicillin-Streptomycin (10,000 U/mL)	Thermo Fisher Scientific	Cat#15140122
DPBS	Thermo Fisher Scientific	Cat#14190144
Recombinant Mouse TNF-α	BioLegend	Cat#718004
Glutaraldehyde 2%	Electron Microscopy Sciences	Cat#16536-05
TRIzol LS Reagent	Thermo Fisher Scientific	Cat#10296028
RT^2 SYBR Green ROX qPCR Mastermix	Qiagen	Cat#330523
Cell Lysis Buffer	Cell Signaling Technology	Cat#9803
Pierce Protease Inhibitor Tablets	Thermo Fisher Scientific	Cat#A32963
Triton X-100	Thermo Fisher Scientific	Cat#85111
PageRuler Plus Prestained Protein Ladder	Thermo Fisher Scientific	Cat#26619
Scientific SuperSignal West Pico PLUS Chemiluminescent Substrate	Thermo Fisher Scientific	Cat#34580
SuperSignal West Atto Ultimate Sensitivity Chemiluminescent Substrate	Thermo Fisher Scientific	Cat#A38556
Normal Goat Serum (10%)	Thermo Fisher Scientific	Cat#50062Z
Formalin solution, neutral buffered, 10%	MilliporeSigma	Cat#HT501128
Hematoxylin QS Counterstain	Vector Laboratories	Cat#H-3404-100
VECTASHIELD HardSet Antifade Mounting Medium	Vector Laboratories	Cat#H-1400-10
Cell-Tak	Corning	Cat#354240
Seahorse XF DMEM assay medium pack	Agilent	Cat#103680-100
Hoechst 33342 Solution	Thermo Fisher Scientific	Cat#62249
Critical commercial assays		
ExoQuick ULTRA EV Isolation Kit for Tissue Culture Media	System Biosciences	Cat#EQULTRA-20TC-1

iScience
iScience
Article

Continued

REAGENT or RESOURCE	SOURCE	IDENTIFIER
ExoQuick ULTRA EV Isolation Kit for Serum and Plasma	System Biosciences	Cat#EQULTRA-20A-1
Thrombin Plasma Prep	System Biosciences	Cat#TMEXO-1
Basic Exo-Flow Capture kit	System Biosciences	Cat#CSFLOWBASICA-1
ExoQuick-TC	System Biosciences	Cat#EXOTC10A-1
EXOCET Exosome Quantitation Kit	System Biosciences	Cat#EXOCET96A-1
RNeasy Mini Kit	Qiagen	Cat#74106
miRNeasy Mini Kit	Qiagen	Cat#217004
RT^2 First Strand Kit	Qiagen	Cat#330404
Pierce BCA Protein Assay Kit	Thermo Fisher Scientific	Cat#23225
Pierce Micro BCA Protein Assay Kit	Thermo Fisher Scientific	Cat#23235
VECTASTAIN Elite ABC-HRP Kit, Peroxidase (Rabbit IgG)	Vector Laboratories	Cat#PK-6101
ImmPACT DAB Substrate Kit, Peroxidase (HRP)	Vector Laboratories	Cat#SK-4105
Seahorse XF Cell Mito Stress Test Kit	Agilent	Cat#103015-100
Experimental models: Cell lines		
Mouse: 3T3-L1 Preadipocytes	ZenBio	SP-L1-F
Human: Subcutaneous Preadipocytes	ZenBio	SP-F-1
Human: HFF-1 cells	ATCC	SCRC-1041
Mouse: RAW 264.7 macrophages	ATCC	TIB-71
Mouse: Cardiomyocytes	Celprogen	Cat#11041-14
Experimental models: Organisms/strains		
Mouse: C57BL/6J	The Jackson Laboratory	RRID:IMSR_JAX:000664
Oligonucleotides		
See Table S5 for the primer sequences	This paper	N/A
Software and algorithms		
ImageJ	Schneider et al.[116]	https://imagej.net/ij/
Spectradyne Data Viewer	Spectradyne	https://nanoparticleanalyzer.com/dlhidgen3/
Vevo LAB 5.8.2	FUJIFILM VisualSonics	https://www.visualsonics.com/product/software/vevo-lab
RT2 qPCR Assay Data Analysis 1808 Spreadsheet	Qiagen	https://www.qiagen.com/us/resources/resourcedetail?id=e08404c0-31e5-4e2f-8daf-c5c651bebf38&lang=en
Image Studio Lite Ver 5.2	LI-COR Biosciences	https://www.licor.com/bio/image-studio/
GraphPad Prism Ver 10	GraphPad Software	https://www.graphpad.com/
Microsoft Excel	Microsoft Corp	https://www.microsoft.com/en-us/microsoft-365/excel
Seahorse Wave Desktop Software	Agilent	https://www.agilent.com/en/product/cell-analysis/real-time-cell-metabolic-analysis/xf-software/seahorse-wave-desktop-software-740897
MultiQuant 3.0.3	AB Sciex	https://sciex.com/products/software/multiquant-software
MetaboAnalyst 5.0	Pang et al.[117]	https://www.metaboanalyst.ca/

(Continued on next page)

Continued

REAGENT or RESOURCE	SOURCE	IDENTIFIER
Other		
Trypomastigotes of *Trypanosoma cruzi* (Brazil strain)	Combs et al.[17]	N/A
Whatman® Puradisc 30 syringe filters	MilliporeSigma	Cat#WHA10462260
Custom RT^2 Profiler PCR Array	Qiagen	Cat#330171
Seahorse XFe96/XF Pro FluxPak Mini	Agilent	Cat#103793-100

RESOURCE AVAILABILITY

Lead contact

Further information and requests for resources and reagents should be directed to and will be fulfilled by the lead contact, Jyothi Nagajyothi (Jyothi.Nagajyothi@hmh-cdi.org).

Materials availability

This study did not generate new unique reagents.

Data and code availability

- All data reported in this paper will be shared by the lead contact upon request. The lipidomics dataset are provided in Supplemental Raw Data file.
- This paper does not report original code.
- Any additional information required to reanalyze the data reported in this paper is available from the lead contact upon request.

EXPERIMENTAL MODEL AND STUDY PARTICIPANT DETAILS

Mammalian cell lines and parasites culturing

Murine 3T3-L1 preadipocytes and Human subcutaneous preadipocytes were purchased from ZenBio. The preadipocytes were differentiated into mature adipocytes by feeding adipocyte differentiation media (murine: for 3 days; and human: for 7 days) and further maintained in adipocyte maintenance media purchased from ZenBio until ready to be assayed. Adipocytes were used between 7-14 days (murine) and 14-21 days (human) post-initiation of differentiation. HFF-1 human foreskin fibroblast and RAW 264.7 murine macrophage cell lines were originally purchased from American Type Culture Collection (ATCC) and maintained as an adherent culture in Dulbecco's Modification of Eagle's Medium (DMEM) supplemented with 10% heat-inactivated fetal bovine serum (HI-FBS) and 1% penicillin/streptomycin. Adult Mouse Cardiomyocytes were purchased from Celprogen and cultured as a monolayer in flasks pre-coated with Adult Mouse Cardiomyocyte Cell Culture Extra-cellular Matrix. Cardiomyocytes were fed with Cardiomyocyte Primary Cell Culture Media with Serum and used for the experiment after 18 hours of plating. All the cell lines were cultured and maintained in a humidified incubator at 37°C and 5% CO_2. Trypomastigotes of *T. cruzi* (Brazil strain) were propagated in HFF cell line and maintained by serial passage in confluent monolayers of HFF cells in DMEM containing 10% HI-FBS and 1% penicillin/streptomycin.[9,118] Trypomastigotes harvested from cell culture supernatants were washed 3 times in cold Dulbecco's phosphate-buffered saline (DPBS) without Calcium and Magnesium by centrifugation, counted and resuspended in warm DPBS at 10^5 parasites per mL and used for *in vitro* and *in vivo* infection experiments.

T. cruzi infection *in vitro*

Cultured murine and human adipocytes were infected with tissue culture-derived trypomastigotes of *T. cruzi* (Brazil strain) at a multiplicity of infection (MOI) of 3:1.[10,17] 24 hours post infection, infected cells were washed twice with warm DPBS to remove excess, unbound parasites and replenished with fresh culture media and incubated for additional 48 hours. Two separate sets of cultured adipocytes (both murine and human) were also included: one set served as uninfected control and the other set was treated with 10ng recombinant TNFα for 48 hours to induce apoptosis. At the experimental end points, the conditioned media (cell culture supernatant) from uninfected, TNFα-treated and *T. cruzi* infected groups of both murine and human adipocytes were collected for adipome isolation. The cells were harvested separately for protein (murine) and mRNA (human) analysis.

Murine model of acute Chagas disease

As males are more prone to develop Chagas cardiomyopathy, only male mice were used in this study. Male C57BL/6J mice, 6-7 weeks old (n=8), were infected intraperitoneally (i.p.) with 1×10^4 tissue culture-derived *T. cruzi* trypomastigotes.[11] A separate group of age- and sex-matched uninfected mice (n=8) were included as controls. Mice were housed at CDI animal research facility in sterilized filter top cages under 12-h light-dark cycle and humidity and temperature-controlled conditions. All animals had *ad libitum* access to water and rodent chow.

Animals were routinely monitored for signs of illness for the entire duration of the study. At 20 days post infection (DPI), both infected and uninfected control mice were euthanized and tissues including heart, visceral fat pads (epididymal white adipose tissue) were harvested along with terminal blood collection.[11,119,120] The experiment was repeated to isolate required amount of adipomes for the functional studies. All animal experiments were conducted in accordance with the National Institutes of Health Guide for the Care and Use of Laboratory Animals with approval from the Institutional Animal Care and Use Committee (protocol #282) of Center for Discovery and Innovation (CDI) - Hackensack University Medical Center.

METHOD DETAILS

Adipome isolation and functional analysis

In vitro adipocytes-derived adipomes

Adipomes released by cultured adipocytes were isolated using ExoQuick-TC Ultra EV isolation kit. The conditioned media from murine and human adipocytes (uninfected, TNFα-treated, *T. cruzi* infected groups) were centrifuged at 3,000 x g for 20 minutes to remove parasites and cellular debris and the supernatants were transferred to new tubes. Additionally, the supernatants were passed through a 1.2 μm syringe filter to remove any parasite contamination in samples. ExoQuick-TC exosome precipitation solution was added to the clarified supernatants at 1:5, mixed thoroughly by inverting the tubes and incubated overnight at 4°C. The samples were then centrifuged at 3,000 x g for 10 minutes to pellet the precipitated EVs. The EV pellets were resuspended and purified by passing through the size exclusion chromatography (SEC) columns provided in the kit following manufacturer's instructions. These purified adipomes were treated on HFF (with human adipocytes-derived adipomes) and RAW (with murine adipocytes-derived adipomes) cells at 1:1 and 1:50 (cell to adipome ratio) for 48 hours and the cells were harvested for mRNA analysis. The adipome numbers were calculated based on the Spectradyne nCS1 measurements.

In vivo white adipose tissue (WAT)-derived adipomes

Adipomes from WAT were isolated and enriched using a combination of ExoQuick-TC Ultra EV isolation kit and Basic Exo-Flow Capture kit as follows. The WATs from infected and uninfected mice were processed separately inside the biosafety cabinet. The harvested tissues were placed in a 12-well plate and gently dissociated in presence of 500 μL cold 1x PBS (sterile) using sterile forceps and scalpel to liberate EVs present in the intercellular spaces. Upon dissociation, the biofluid was passed through 70 μm cell strainer to remove large chunks of tissue and flushed with additional 500 μL of cold PBS. The biofluid was then centrifuged at 500 x g for 10 mins to remove cell debris at 10°C. The supernatant was transferred to a new tube and re-centrifuged at 21,000 x g for an hour at 10°C. After completion of the spin, the supernatant was carefully transferred again to a new tube without disturbing the pellet and/or the white precipitates smeared on the inner sides of the tube, if using fixed-angle rotor. The pellet/precipitate was resuspended in 250 μL PBS. Then, the ExoQuick-TC exosome precipitation solution was added to both the resuspended pellet and supernatant fraction at 1:5, mixed thoroughly by inverting the tubes and incubated overnight at 4°C. On the following day, the samples were centrifuged at 3,000 x g for 10 minutes to pellet the precipitated EVs and further purified using the SEC columns as detailed above. The EVs from resuspended pellets were referred as large-EVs (L-EV) while the supernatant derived EVs were referred as small-EVs (S-EV). Next, L-adipomes and S-adipomes were enriched from L-EV and S-EV, respectively utilizing adipocytes-specific antibody cocktail (0.5 μg/assay biotinylated mouse adiponectin antibody and 0.5 μg/assay biotinylated mouse FABP4 antibody) and magnetic streptavidin 9.1 μm Exo-Flow bead system following manufacturer's instructions with slight modification to improve recovery. Adipomes enriched from control uninfected L-EV and S-EV were referred as CLA and CSA, respectively. Whereas adipomes from infected L-EV and S-EV were referred as ILA and ISA, respectively. Washed bead-bound adipomes were sent for lipidomics analysis (Georgetown University Metabolomics Center). The protein from magnetic bead bound adipomes were extracted directly by on-bead lysis (using 0.25% Triton X-100 followed by sonication and used for method validation by western blot and qPCR analyses. The eluted adipomes were reprecipitated with ExoQuick-TC precipitation buffer for 2 hours at 4°C to remove the elution buffer, centrifuged at 3,000 x g for 20 minutes at 10°C, resuspended in 1x PBS and used for adipome characterization (size, distribution, concentration TME) and functional analyses in murine RAW macrophages and primary cardiomyocytes.

Plasma-derived adipomes

Adipomes were isolated from uninfected and *T. cruzi* infected mice plasma in a similar fashion as described above using ExoQuick Ultra EV isolation kit for serum/plasma with the addition of thrombin treatment. Plasma-derived Infection-associated L-adipomes (P-ILA) were injected to C57BL/6J mice and analyses including Cardiac Ultrasound imaging, histological examination of heart tissue and protein analysis were performed.

EXOCET assay

The amount of WAT-derived large-EVs and small-EVs were quantified using EXOCET Exosome Quantification kit following manufacturer's instructions. The assay measures the activity of Acetyl-CoA Acetylcholinesterase (AChE), an enzyme highly enriched in exosomes.[121]

Immunofluorescence analysis

Adipocyte staining

Murine 3T3-L1 adipocytes were grown and differentiated on glass coverslips and treated with 10ng recombinant TNFα for 24 hours. The cells were fixed overnight with 4% paraformaldehyde for 2 hours, washed three times in PBS and blocked with 10% goat serum for 30 minutes at room temperature to minimize non-specific adsorption of antibodies. The cells were then stained with a combination of mouse monoclonal Adiponectin and rabbit monoclonal Annexin V primary antibodies in one set and goat polyclonal FABP4 and rabbit monoclonal Annexin V primary antibodies in another set for an hour at room temperature. Followed by secondary staining with appropriate Alexa Fluor antibody combination: Goat anti-mouse IgG Alexa Fluor 488 and Goat anti-rabbit IgG Alexa Fluor 594 for the first set and Donkey anti-goat IgG Alexa Fluor 594 and Goat anti-rabbit IgG Alexa Fluor 488 for the second set. The coverslips were washed and mounted with VECTASHIELD HardSet Antifade Mounting Medium. Samples were then imaged on Nikon Eclipse Ti2 Epi-fluorescence microscopy (Nikon Instruments Inc).

Adipome staining

WAT-derived adipomes were bound to magnetic streptavidin 9.1 μm Exo-Flow beads conjugated to Adiponectin/FABP4 antibody as detailed in adipome isolation section. The adipome-bound beads were washed twice with PBS and parted in two halves. One fraction was stained with mouse monoclonal Adiponectin antibody followed by secondary staining with Goat anti-mouse IgG Alexa Fluor 488. The other fraction was stained with rat monoclonal FABP4 antibody followed by secondary staining with Goat anti-rat IgG Alex Fluor 488. A third tube containing untouched magnetic streptavidin beads alone was stained with a mix of Goat anti-mouse and anti-rat IgG Alexa Fluor 488 and used as control. The stained beads suspended in PBS were spotted on a glass slide and mounted using coverslip with VECTASHIELD HardSet Antifade Mounting Medium. The beads were imaged on Nikon Eclipse Ti2 Epi-fluorescence microscopy equipped with a Nikon Plan Fluor 100x/1.30na objective.

Nanoparticle Tracking

Spectradyne nCS1 instrument was used to evaluate the size and concentration of adipocytes-derived EVs/adipomes. Cultured murine and human adipocytes-derived adipomes were analyzed using C-900 cartridges with a size detection range of 130-900 nm particle diameters. Whereas, WAT-derived adipomes were analyzed using C-2000 cartridges with size detection range of 250-2000 nm. In all cases, samples were prepared by mixing 9 μL of purified adipomes with 1 μL of 0.02 μm filtered 10x PBS-T to increase sample conductivity. Out of which, 5 μL samples were loaded onto the cartridges and primed in the instrument using 0.2 μm filtered 1x PBS-T. Particle acquisition was performed on continuous mode until count reaches a set stop point of 2000 particles with <2.5% statistical error. The acquired stats files were analyzed for particle size distribution and concentration (per mL) using Spectradyne Data Viewer software and to generate peak-filtered, background subtracted CSD plots.

Transmission electron microscopy

Transmission electron microscopy (TEM) images of L-adipomes and S-adipomes were obtained at the analytical imaging facility - Albert Einstein College of Medicine. Adipome samples were fixed with 2% Glutaraldehyde in 0.1M Phosphate Buffer and stored at 4°C. 400 mesh, carbon only grids were plasma cleaned using a Tergeo-EM Plasma Cleaner (PIE Scientific). Fixed adipome suspension were adsorbed onto grids for 10 mins and wicked dry. Samples were then negatively stained with 1% aqueous uranyl acetate and viewed on a Tecnai 20 transmission electron microscope (ThermoFisher Scientific) operating at a voltage of 120 kV. Acquired images were saved in high resolution TIFF format.[122,123]

Cardiac ultrasound imaging

Male C57BL/6J mice, 6-7 weeks old (n=6) were treated with P-ILA (1x10^9 adipomes suspended in 40ul 1x PBS) or vehicle (1xPBS) through ultrasound-guided intracardiac injections using a Vevo 3100 preclinical imaging system. Ultrasound-guided injections were performed twice a week to administer adipomes/vehicle into left ventricle wall.[124] Cardiac Ultrasound Imaging of the hearts were performed 4 days after the second dose of adipome administration.[11] In another experiment, mice (n=10) were first infected intraperitoneally with 1x10^3 trypomastigotes of *T. cruzi*.[11] Infected mice were then treated with P-ILA (1x10^9 adipomes suspended in 40ul 1x PBS) or vehicle (1xPBS) after 35 days post infection (DPI) by intracardiac injections. A separate group of age- and sex-matched uninfected mice (n=8) were included as controls and treated with either P-ILA or vehicle. B-mode, M-mode, and pulse wave Doppler image files were collected from both the parasternal long-axis and short-axis views. Morphometric measurements were determined using the Vevo LAB ultrasound analysis software.

Histological analysis

Mice heart tissues were collected 10 days after the first P-ILA administration. A portion of the freshly isolated tissues were fixed with 10% neutral-buffered formalin for a minimum of 48 hours and then embedded in paraffin wax. Hematoxylin and eosin and Picrosirius red staining were performed, and the images were captured.[11] Immunohistochemistry (IHC) was performed on the formalin-fixed heart sections using rabbit polyclonal ANP antibody and rabbit polyclonal TNFα antibody with a dilution of 1:250 and 1:200, respectively, followed by biotinylated secondary antibody using VECTASTAIN Elite ABC-HRP kit. The sections were then washed and incubated with peroxidase substrate and

counterstained with hematoxylin. Four to six images per section were captured and quantification of DAB positive staining intensity was performed using the image processing and analysis tool ImageJ.

Immunoblotting analysis

Murine 3T3-L1 adipocytes (uninfected, TNFα-treated and *T. cruzi* infected) were washed twice with cold PBS followed by incubating on ice with 400 μL of 1x lysis buffer containing Pierce protease inhibitor cocktail for 10 minutes. The cells were then scraped off and transferred to a sterile tube and sheared by passing through 28G1/2 insulin syringe for ten times. The cell lysates were centrifuged for 20 minutes at 14,000 x g in a cold microfuge and the clarified supernatants were recovered in new tubes. Mice WAT and heart tissues (uninfected, infected, and adipome treated) were homogenized using a handheld homogenizer after adding appropriate volume of 1x lysis buffer with protease inhibitor cocktail. The homogenates were then incubated on ice for 10 minutes followed by centrifugation and supernatant recovery as mentioned above. The protein concentration was quantified using Pierce BCA protein quantification kit. 30 μg total protein from each sample were treated with 2-Mercaptoethanol, reducing agent and heat denatured at 100°C for 5 minutes before resolving on SDS-PAGE. Protein from cultured adipocytes-derived and WAT-derived adipomes were prepared by lysing the samples with 0.25% Triton X-100 v/v and sonicating the sample tubes in an ultrasonic water bath for 10 minutes on high frequency setting. Adipome protein concentration was quantified using Pierce Micro BCA protein assay kit. Samples were reduced, heat denatured and resolved on SDS-PAGE as mentioned earlier. PageRuler Plus Prestained protein ladder was used as size standards in SDS-PAGE. The proteins were then transferred onto nitrocellulose membrane for immunoblot analysis. Primary antibodies against Caspase 7, Cleaved Caspase 7, Annexin V, Phospho-Perilipin 1, Adiponectin, Perilipin 1, FABP4, β1-Adrenergic Receptor, CHOP, TNFα, IFNγ, IL6, F4/80, SREBP, PPARα, SDHA, Cytochrome c, COX IV, HSP60, BiP, Phospho-eIF2α, PDI, and BNIP3 were used to detect the expression of corresponding proteins. β-Actin and Guanosine nucleotide dissociation inhibitor were used as appropriate control to assess equal protein loading. Horseradish peroxidase (HRP)-conjugated anti-mouse immunoglobulin, HRP-conjugated anti-rabbit immunoglobulin and HRP-conjugated anti-rat immunoglobulin were used as appropriate secondary antibodies to detect chemiluminescent signal using SuperSignal West Pico PLUS or SuperSignal West Atto Ultimate Sensitivity substrate on the Invitrogen iBright Imaging Systems. All the densitometric analyses of the target protein bands on the immunoblots were analyzed with the Image Studio lite package Ver 5.2 (LI-COR Biosciences).

RNA extraction and quantitative PCR

Cultured human adipocytes (uninfected, TNFα-treated and *T. cruzi* infected) and adipomes treated human fibroblasts, RAW macrophages and murine cardiomyocytes were subjected to total RNA isolation using RNeasy mini kit according to manufacturer's instructions. 0.5 to 1 μg of total RNA was used for reverse transcription and cDNA synthesis using RT² First Strand Kit after genomic DNA elimination as per manufacturer's instructions. The cDNA samples were diluted at 1:5 and quantitative PCR (qPCR) experiments were performed using RT² SYBR Green ROX Mastermix following manufacturer's instructions. All assays were performed on Applied Biosystems QuantStudio 3 Real-time PCR System according to the following cycling conditions: 10 minutes at 95°C (1 cycle, HotStart DNA Taq Polymerase activation), followed by 15 seconds at 95°C and 1 minute at 60°C (40 cycles, PCR amplification and data collection). Dissociation (melting) curve analysis was added to the run set up by enabling default melting curve program to verify PCR specificity. Data analysis was performed normalized to the expression of HPRT and/or GAPDH using the ΔΔCT method and the mRNA expression (fold change) levels were plotted as bar graphs.

Custom RT2 Profiler Real-Time PCR array for mouse genes involved in adipogenesis, lipogenesis, cellular metabolism-specific signaling molecules and markers of immune and inflammatory responses was used to analyze gene expression in RAW macrophages treated with L- and S-adipomes of uninfected and *T. cruzi* infected mice for 48 hours. Data analysis was performed normalized to the expression of Hprt using the ΔΔCT method and statistical analysis was performed as suggested using RT2 qPCR Assay Data Analysis 1808 Spreadsheet from Qiagen.[26,68]

Total RNA from adipomes were extracted using TRIzol LS reagent and purified using miRNeasy Mini kit following manufacturer's instructions. The total yield was used for reverse transcription and cDNA synthesis as mentioned above. PCR was performed with undiluted cDNA samples to analyze the presence of adipogenic genes, apoptotic and EV-specific marker genes within adipomes. The PCR product was resolved on 2% agarose gel and imaged using the Invitrogen iBright Imaging Systems.

For quantitative determination of parasite load in P-ILA treated heart, a standard curve PCR was performed using the *T. cruzi* DNA standard (ranging from 31.2pg to 0.002pg) along with DNA samples extracted from mice heart tissue.[17] Complementary DNA made from RNA isolated from *T. cruzi* infected 3T3-L1 adipocytes (as positive control) and P-ILA treated cardiomyocytes were also included in the PCR.

Lipidomics analysis

All LC-MS grade solvents including acetonitrile and water were purchased from Fisher Scientific. High purity formic acid (99%) was purchased from Thermo Fisher Scientific. EquiSPLASH LIPIDOMIX quantitative mass spec internal standard and 15:0-18:1-d7-PA, C15 Ceramide-d7 (d18:1-d7/15:0) and 18:1 Chol (D7) ester were purchased from Avanti polar lipids. Internal standard for free fatty acid (FFA), dihydroceramides (DCER), hexosylceramides (HCER), lactosylceramides (LCER) were purchased from Sciex as Lipidyzer platform kit. This method was designed to measure 21 classes of lipid molecules which includes diacylglycerols (DAG), chloesterol esters (CE), sphingomyelins (SM), phosphatidylchloine (PC), triacylglycerols (TAG), free fatty acids (FFA), ceramides (CE), dihydroceramides (DCER), hexosylceramide (HCER), lactosylceramide (LCER), phosphatidylethanolamine (PE), lysophosphtatidylchloine (LPC), lysophosphatidylethnolamine (LPE), phosphatidic acid (PA),

lysophosphatidic acid (LPA), phosphatidylinositol (PI), lysophosphotidylinositol (LPI), phosphatidylglycerol (PG), acylcarnitines and phosphatidylserine (PS) using QTRAP 5500 LC-MS/MS System (Sciex) as detailed below.

The adipomes (CLA, ILA, CSA and ISA) bound to magnetic beads were suspended in 1xPBS (40ul). Repeated freeze thaw cycles followed by sonication for 30 sec was performed to release the contents of adipome cargoes into suspension. To the above solution, 100 μL of chilled isopropanol containing internal standards for lipids was added and the samples were vortexed and kept on ice for 20 minutes. Samples were incubated at -20°C for 20 minutes and then centrifuged at 13,000 rpm for 20 minutes at 4°C. The supernatant was transferred to MS vial for LC-MS analysis. 5 μL of each sample was injected onto a Xbridge amide 3.5 μm, 4.6 X 100 mm (waters) using SIL-30 AC auto sampler (Shimazdu) connected with a high flow LC-30AD solvent delivery unit (Shimazdu) and CBM-20A communication bus module (Shimazdu) online with QTRAP 5500 (Sciex) operating in positive and negative ion mode. A binary solvent comprising of acetonitrile/water 95/5 with 10 mM ammonium acetate as solvent A and acetonitrile/water 50/50 with 10 mM ammonium acetate as solvent B was used for the resolution. Lipids were resolved at 0.7 mL/min flow rate, initial gradient conditions started with 100% of solvent A, shifting towards 99.9% of solvent A over a time period of 3 minutes, 94% of solvent A over a time period of 3 minutes and 25% of solvent A over a period of 4 minutes. Finally, washing with 100% of B for 6 minutes and equilibrating to initial conditions (100% of solvent A) over a time period of 6 minutes using auto sampler temperature 15°C and oven temperature 35°C. Source and gas setting were as follow: curtain gas = 30, CAD gas = medium, ion spray voltage = 5.5 kV in positive mode and −4.5 kV in negative mode, temperature = 550°C, nebulizing gas = 50 and heater gas = 60. The data were normalized to respective internal standard area for each class of lipid and processed using MultiQuant 3.0.3 (Sciex). The quality and reproducibility of LC-MS data was ensured using a number of measures. The column was conditioned using the pooled QC samples initially and were also injected periodically to monitor shifts in signal intensities and retention time as measures of reproducibility and data quality of the LC-MS data. NIST plasma sample prepared in the same manner was also ran alongside to check for the instrumental variance. Additionally, blank solvent runs were performed between set of samples to minimize carry-over effects. Lipidomics data were provided in the form of normalized response which was area under the curve for each metabolite divided by internal standard area. Lipid data was preprocessed using signal/noise > 20:1 and retention time (RT) tolerance 5 seconds. Analysis yielded 287 reliable features in the adipome samples under study. The quality of data was monitored based on coefficient of variation (CV) of each lipid in pooled QC samples, the lipids having CV>20% were filtered off. The figures were generated using MetaboAnalyst 5.0.

Magnetic resonance imaging (MRI)
Cardiac gated MRI was performed on murine model of acute Chagas disease along with uninfected controls using a 9.4T Varian Direct Drive animal magnetic resonance imaging and spectroscopic system (Agilent Technologies).[8,68]

Seahorse XF96 cell metabolic analysis
The mitochondrial function of cardiomyocytes upon plasma-derived adipome treatments was assessed by Seahorse XFe96 analyzer, using the Seahorse XF Cell Mito Stress Test kit. Mouse cardiomyocytes were treated with vehicle, P-CLA, and P-ILA at 1:20 (cell to adipome) ratio for 48 hours before assessing their mitochondrial function. A day prior to the assay, the adipome treated cells were plated on to a Cell-Tak coated XFe96 cell culture microplate at a seeding density of 20,000 cells/well, supplemented with cardiomyocyte culture media and incubated overnight at 37°C in 5% CO_2 incubator. The XFe96 sensor cartridge was hydrated overnight with sterile water in a humidified non-CO_2 37°C incubator and then submerged in pre-warmed XF-calibrant for 45–60 min prior to loading drug ports. On the day of the assay, the cells were supplied with Seahorse assay medium (XF DMEM medium pH 7.4, 10 mM XF Glucose, 2 mM XF Glutamine, 1 mM XF Pyruvate). For determination of mitochondrial respiration, 1.5 μM Oligomycin, 0.5 μM FCCP, and 0.5 μM Rotenone/AA were prepared in assay medium and added to the ports A, B, and C on the sensor cartridge, respectively. Mitochondrial function was assessed in real time following the injection of Oligomycin, FCCP, and Rotenone/AA according to the default measurement protocol. Data were normalized to nuclear content by staining the live cells with Hoechst 33342 after the assay and fluorescence cell counting using Biotek Cytation C10. The normalized data was then exported to the report generator to create graphs.

QUANTIFICATION AND STATISTICAL ANALYSIS
Statistical analyses were performed using GraphPad Prism Ver 10.0 (GraphPad Software, LLC) or Microsoft Excel (Microsoft Corp). Comparisons between groups were made using Two-Way ANOVA and unpaired Student's t-test as appropriate for western blotting data analysis. For custom RT2 Profiler array, the analysis was performed using Qiagen RT2 qPCR Assay Data Analysis 1808 Spreadsheet and the p values were calculated based on Student's t-test. Fold-regulation (up or down) was plotted on Microsoft Excel. Statistical analysis of other qPCR experiments was performed using Microsoft Excel and the comparisons between the groups were analyzed using unpaired Student's t-test. Significant differences were reported for p values between ≤ 0.0001 and < 0.05 with symbols (*/#) as appropriate. Data represent means ± S.E.M. For lipidomics, statistical analysis between the groups was done using MetaboAnalyst 5.0.